Effect of cold drawing reduction rate on edge-to-center-characterized microstructure and orientation alongside residual stresses in conjunction with magnetic properties of low-carbon high-alloy ferromagnetic steel

Shahab Bazri [a],[*], Carlo Mapelli [a],[*], Silvia Barella [a], Andrea Gruttadauria [a], Davide Mombelli [a], Renato Nemfardi [b], Roberto Bedini [b], Giorgio Zucchelli [b]

[a] *Department of Mechanical Engineering, Politecnico di Milano 20156 Milan, Italy*
[b] *Eure Inox srl, Via Leonardo Da Vinci, 2 20068 Peschiera Borromeo MI, Italy*

ARTICLE INFO

ABSTRACT

In the current research, the effect of cold drawing reduction rate (CDRR) of 15% and 45% and the required subsequent isothermal static recrystallization annealing heat treatment (ISRAHT) on the microstructures, textures, residual stresses, and magnetic properties of ferritic/ferromagnetic stainless steel (FSS), EN 1.4106, are investigated by a series of experimental analyses. The study is carried out by the theoretical well-known model of Johnson-Mehl-Avrami-Kolmogorov (JMAK) in conjunction with aforesaid properties. According to the results, by increasing the CDRR, the recrystallization fractions (RF) become faster in accordance with the JMAK theory. Such an increment also affects more fragmented and elongated grains, which leads to provide smaller grains in size. However, by the effect of slow cooling process (SCP), the grain growth is another noticeable part of study. Likewise, the effects of CDRR and the subsequent ISRAHT find to be beneficial for the evolution of microstructures, textures, and relief of residual stresses, and better performance of magnetic behavior. For instance, higher relative magnetic permeabilities approximately above 1000 causes to reach residual stresses closer to zero. The cold-drawn FSSs are consisted of the α-fibre texture, which is close to $\{223\}\langle110\rangle$ and $\{111\}\langle110\rangle$, with higher intensity while by gradual higher recrystallization, the orientation tendency to $\{111\}\langle011\rangle$ of γ-fibre are formed following to the more distributed texture with lesser intensity. The findings display that while the recrystallization process addresses the formation of new grains, resulting in the more equiaxed grains, more well-aligned textures are also achieved in respect to the lower misorientation uniformity density and even with more distributed clusters.

1. Introduction

Ferritic stainless steels (FSS) with 11% to 30% chromium content, basically known as Fe-Cr-Mo [1] or more theoretically concise as Fe-Cr binary alloys [2,3], have economically lower cost versus austenite owing to the Ni absence [4], while they are also particularly ferromagnetic (magnetically soft steels), which is a vital benefit for several applications such as the solenoid valves/fittings, electrovalves, and electromagnetic pumps that are the main target applications of the current research as well. Moreover, they are widely utilized in the automobile exhaust system [5] (petrol/diesel injectors), petroleum, the household appliances and so on [6,7]. As a result, they are mainly a major economical civil field [8]. However, the foremost deficiency of FSS is their dependence on the mechanical properties for varied temperatures, such as stress-subjected mechanical brittleness at room temperature or even higher levels for FSS [9]. This drawback causes to limit the production and applications [10]. It is evident that the heat treatment and cooling procedures are quite determinative for the required properties of the final product in each case of applications [11] owing to the evolution of microstructures and textures as well [12].

Unlike martensitic grades, FSS grades are not able to be stiffened by the quench hardening but only through cold working processes such as cold wire drawing. In addition, for enhancement of the microstructures and mechanical behavior of FSS, enormous studies have been conducted based on the cold rolling and/or drawing as well as the subsequent annealing process [13]. By this way, the microstructural adjustment through optimization and/or comparison approaches have been

Nomenclature

Abbreviations/acronyms

AGS	Average grain size
AIT	Annealing incubation time
AST	Annealing soaking temperature
CD	Cold-drawn
CDRR	Cold-drawn reduction rate
DD	Dislocation density
EBSD	Electron backscatter diffraction
FSS	Ferritic stainless steel
GB	Grain boundary
HAGB	High angle grain boundary
IPF	Inverse pole figure
ISRAHT	Isothermal static recrystallization annealing heat treatment
JMAK	Johnson-Mehl-Avrami-Kolmogorov
LAGB	Low angle grain boundary
ND	Normal direction
OM	Optical microscopic
OP	Pole figure
RD	Rolling direction
RF	Recrystallization fraction
RMP	Relative magnetic permeability
RR	Reduction rate
SCP	Slow cooling process
SS	Stainless steel
TD	Transverse direction
TRAM	Temperature ratio of annealing over melting point
XRD	X-ray diffraction

Symbols

d	Interplanar distance/space
E	Young's modulus
HcJ	Coercive field or coercivity (KAm^{-1})
J	Magnetic polarization
k	A constant
L	Diffractometer's coordinates
n	The JMAK exponent
S	Textural constant
t	Time (s)
T	Temperature
X	The recrystallized fraction

Greeks

$K\alpha$	Wavelength of radiation type
ε	Strain
μ	Magnetic permeability
ν	Poisson's ratio
ρ	Density
σ	Stress
τ	Shear stress
θ	Misorientation angle
Φ	Diameter
φ	Offset rotation angle of XRD goniometer
ψ	Diffraction/scattering angle

Subscripts and superscripts

max	Maximum
min	Minimum
r	Relative

reported as well that was mentioned by [14]. To this end, the evolution of microstructure of cold-worked FSS after recrystallization annealing conditions has been also investigated by different studies. There is no need to explain that such researches focusing on cold-worked and heat-treated condition have been done for other grades of stainless steels as well [15,16]. Consideration of different temperature and time for annealing heat treatment have been an extensive part of this research avenue. However, there are several criteria that have been hinted by different studies. For instance, one of the reasons that the annealing temperature cannot be applied for higher degrees is for avoiding lower toughness at the room temperature [17]. On the other hand, in case of cold working processes, the residual stresses are generated. The residual stresses basically define the strength of materials and also cracking susceptibility states [18]. For example, a state of compressive stress on the surface layer can diminish the risk of cracking whereas the tensile stress state can augment the development of cracking.

Moreover, in order to investigate the phase transformation kinetics, recrystallization kinetics, the grain growth, texture formation, and precipitations analyses, the JMAK theory is employed for various materials, which has been reported by enormous papers such as [19]. Relating to the main references of [20–22], the governing JMAK model is as follows:

$$X = 1 - \exp(-kt^n) \tag{1}$$

where X, t, k, and n specify the recrystallized fraction, the time, a constant, and the JMAK kinetic exponent, respectively, while also the preceding investigations implies that the n value corresponds to the growth direction of grains.

In the current study, the effect of isothermal static recrystallization annealing heat treatment (ISRAHT) on the evolution of microstructure, texture, and residual stresses as well as the magnetic behavior of low carbon and medium chromium content EN1.4106 ferritic/ferromagnetic stainless steel after different cold drawing reduction rates has been investigated. To this end, different annealing conditions, including three various annealing soaking temperature and seven different incubation time were taken into account. The improved magnetic properties and relaxation of residual stresses have been deliberated through microstructural observations. This research is supposed to optimize a part of
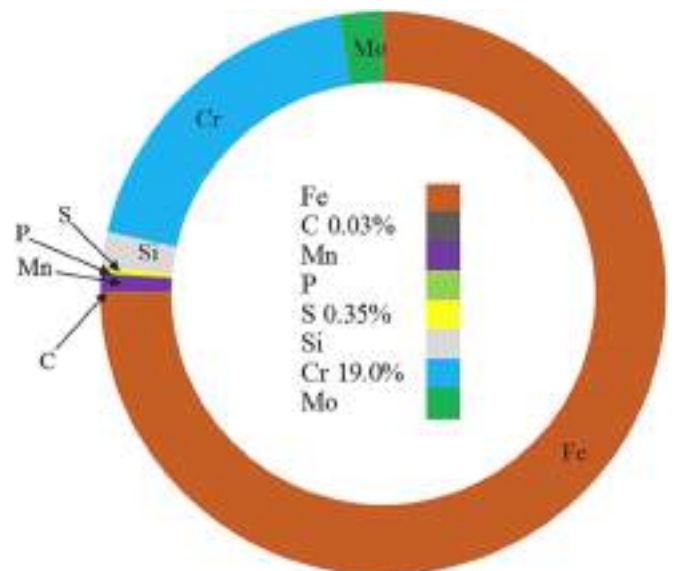

Fig. 1. The chemical compositions of the chosen ferritic/ferromagnetic stainless steel grade, EN 1.4106.

Table 1
Diffraction status table for the measurement of residual stresses.

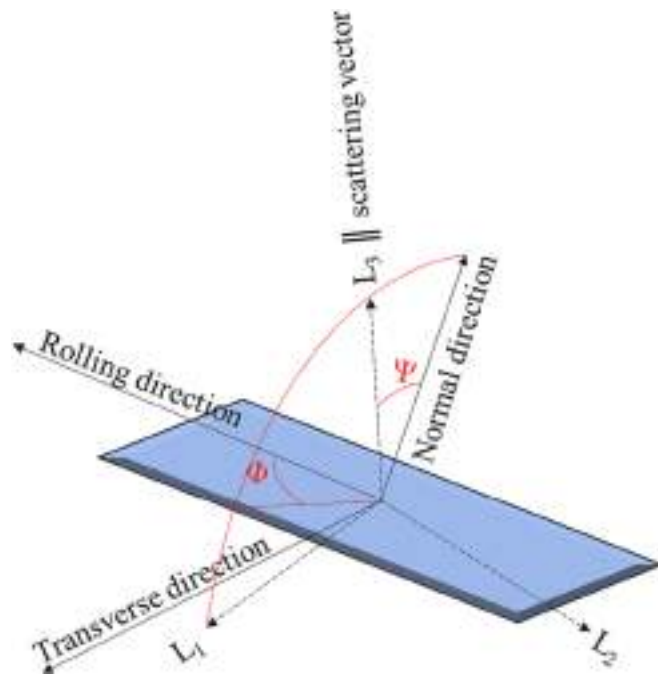| Diffraction conditions	Main settings	No.87	N0.49	No.88	N0.55
Material	FSS	Cold-drawn, 45% RR	Annealed, 96.4% RF	Cold-drawn, 15% RR	Annealed, 74.9% RF
X-ray tube	Cr				
Wavelength	$K\alpha1 = 0.22897$	Using $K\alpha = 0.2291$			
	$K\alpha1 = 0.229361$				
{hkl} for stress measurements	{211}				
Scattering/diffraction angle off FSS at different offset rotation	156.1°	$\varphi = 0°$: 154.35°	$\varphi = 0°$: 154.66°	$\varphi = 0°$: 154.41°	$\varphi = 0°$: 154.65°
		$\varphi = 45°$: 154.37°	$\varphi = 45°$: 154.66°	$\varphi = 45°$: 154.43°	$\varphi = 45°$: 154.60°
		$\varphi = 90°$: 154.43°	$\varphi = 90°$: 154.66°	$\varphi = 90°$: 154.44°	$\varphi = 90°$: 154.54°

Fig. 2. Orientation of the diffractometer's system (based on the working status of collimator and goniometer as the local laboratory's coordinates), *L*, (*L₂* lying on the surface of specimen and the scattering vector is shown by *L₃*) with reference to the specimen's coordinates *RD*, *TD* and *ND*. The ϕ and ψ angles are accordingly defined by the direction the specimen's frame.

the industrial-based annealing production line for the aforementioned applications in the stainless steel market.

2. Materials and methods

The elemental composition of the cold-drawn stainless steel round bars of 19Cr-0.35S-0.03C, known as EN 1.4106, using in the current study, supplied by Eure Inox srl Company has been depicted in Fig. 1. Two diameters of 9 mm and 11 mm with different reduction rates (RRs) of 45% and 15%, respectively, were chosen.

Furthermore, the ISRAHT without phase transformation was accomplished to the cold-drawn (CD) or unheated specimens. Different annealing conditions, comprising of three set temperature ratios of 0.65, 0.68, and 0.71, defining as a temperature ratio between the annealing temperature over melting point of the material (TRAM), which is expressing in equation (2), were considered. The annealing temperature aimed at glowing the material below the critical temperature during a set of seven different incubation time, providing 42 unique samples, in order to evaluate the microstructural observation at different recrystallization fractions. 5, 15, 30, 60, 120, 240, and 480 min for 45% RR as well as 10, 20, 40, 80, 160, 320, 640 min for 15% RR were determined for the annealing incubation time.

$$TRAM = \frac{T_{Annealing}}{T_{MeltingPoint}} \quad (2)$$

2.1. Theoretical framework and methodology for residual stress measurement

To begin with, the theoretical part of stress calculations is described by owing to the methodology of residual stresses in accordance with the European standard, EN 15305, to be analyzed by X-ray Diffraction (XRD) method. An X-ray diffractometer of Stresstech, X-STRESS 3000, with a chromium tube (as the ferrite reference) was used for the tests of residual stresses while the diffraction conditions were indicated in Table 1. In this research, the second order equations of stress calculation was considered for the measurements. Nonlinear $sin^2\psi$ diffraction approach was used to determine interplanar spacing, $d_{\phi\psi}$, in terms of various orientations (Fig. 2) [23,18].

The strain, ε, in a defining direction by ϕ and ψ, specifying the rotation angle and the diffraction/scattering angle, respectively, following by the textural sets of the planes, {hkl};

$$\varepsilon_{\phi\psi}^{\{hkl\}} = S_1^{\{hkl\}}[\sigma_{11} + \sigma_{22} + \sigma_{33}] + \frac{1}{2}S_2^{\{hkl\}}\sigma_{33}cos^2\psi$$
$$+ \frac{1}{2}S_2^{\{hkl\}}[\sigma_{11}cos^2\phi + \sigma_{22}sin^2\phi + \tau_{12}sin2\phi]sin^2\psi \quad (3)$$
$$+ \frac{1}{2}S_2^{\{hkl\}}[\tau_{13}cos\phi + \tau_{23}sin\phi]sin2\psi$$

where the two textural constants S_1 and S_2 m are defined by the Poisson's ratio, v, and Young's modulus, E:

$$\frac{1}{2}S_2^{\{hkl\}} = \frac{1+v}{E} \quad (4)$$

$$S_1^{\{hkl\}} = \frac{-v}{E} \quad (5)$$

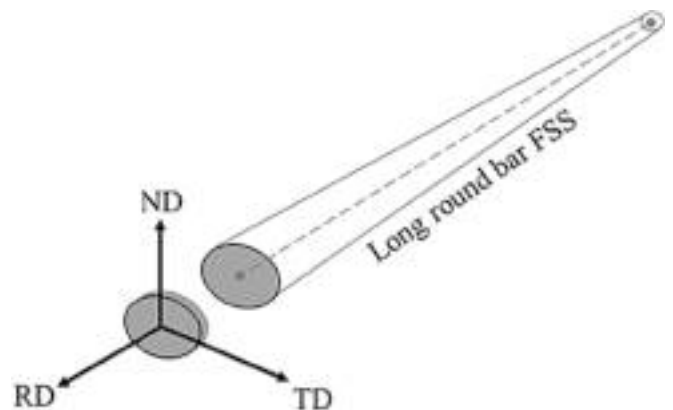Following the stress components of, σ_ϕ, the main stress, as well as, τ_ϕ,

Fig. 3. Schematic figure of the round bar specimens cutting along the RD for the microstructural analysis.
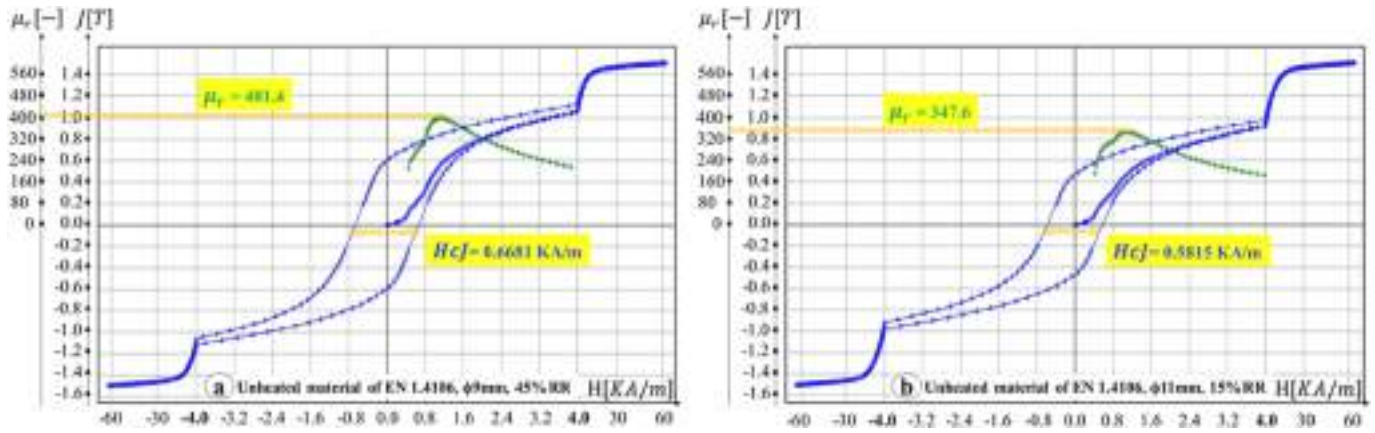
Fig. 4. The results of magnetic hysteresis loops for the cold-drawn specimens, including with a) 45% RR and b) 15% RR.

the shear stress, referring to the Dölle-Hauk method:

$$\sigma_\phi = [\sigma_{11}cos^2\phi + \sigma_{22}sin^2\phi + \tau_{12}sin2\phi] \qquad (6)$$

$$\tau_\phi = [\tau_{13}cos\phi + \tau_{23}sin\phi] \qquad (7)$$

while the strain is approximated by:

$$\varepsilon_{\phi\psi} = \frac{d_{\phi\psi} - d_0}{d_0} \qquad (8)$$

where d_0 is an interplanar spacing under condition of zero, and by assuming the value of σ_{33} ignorable as zero, the interplanar spacing, $d_{\phi\psi}$:

$$d_{\phi\psi} = d_0 + \frac{1}{2}S_2d_0\sigma_\phi sin^2\psi + \frac{1}{2}S_2d_0\tau_\phi sin2\psi \qquad (9)$$

In respective to the model of Dölle-Hauk:

$$d = d_0 + \frac{1}{2}S_2d_0\sigma_\phi sin^2\psi + \frac{1}{2}S_2d_0\tau_\phi sin2\psi = a_1 + a_2 \qquad (10)$$

The calculations of the stresses at 3 angles of 0, 45, and 90° (based on the directions of the XRD settings):

$$\sigma_{11} = \sigma_{0°}$$

$$\sigma_{22} = \sigma_{90°}$$

$$\tau_{12} = \sigma_{45°} - \frac{\sigma_{0°} + \sigma_{90°}}{2} \qquad (11)$$

In the end, the principal maximum and minimum stresses are calculated as:

$$\sigma_{max} = \frac{\sigma_{11} + \sigma_{22}}{2} + \sqrt{\left(\frac{\sigma_{11} - \sigma_{22}}{2}\right)^2 + \tau_{12}^2} \qquad (12)$$

$$\sigma_{min} = \frac{\sigma_{11} + \sigma_{22}}{2} - \sqrt{\left(\frac{\sigma_{11} - \sigma_{22}}{2}\right)^2 + \tau_{12}^2} \qquad (13)$$

2.2. Procedure of magnetic properties measurement

Two magnetic properties (permeability and coercivity) of all defined 44 specimens, containing unheated and heat-treated, were considered for the selection of more critical samples to attain the evolution of the most plausible diversity of the microstructures in the current industrial-based study. KOERZIMAT 1.097 HCJ, FOERSTER, as a commercial type of magnetometer equipment, supplied by Eure Inox srl was used to measure magnetic examinations. The reference measurement was set by 30 KA.m^{-1} at room temperature. The required and accurate length of the bars was cut in relevant to the precise nominal diameters to be tested

by the equipment. To this end, the minimum, median, and maximum values for all six 7-unique-sample series, defining the same annealing temperature and the same reduction rate but various incubation time in each series, were measured for the subsequent EBSD analyses. Due to the normal fluctuation of the magnetic results, the repeatability and reproducibility of the measurements must be taken into account.

2.3. Microstructural characterization method

The advanced characterization method of electron backscattered diffraction (EBSD) was used for the microstructural and textural analyses on the cross-section of the samples along the rolling direction (RD) or longitudinal direction on the plane of transverse and normal directions (TD and ND) for the unheated and heat-treated specimens (Fig. 3). However, the optical microscopic (OM) technique was also employed for the coverage of the undetected samples by EBSD.

As for the EBSD observations, the extra steps of surface polishing, containing automatic mirror polishing (from coarse, fine, and ultra-fine polishing) of 3 and 1 μm with subsequent usage of non-colloidal silica, plus vibro-polishing and electro-polishing were carried out. EBSD approach was applied for the selected specimens according to the magnetic tests, which will be discussed later on, upon the core, edge, and a radial strip region. The EBSD analyses were conducted by an Oxford Instruments machine with a C-Nano-type camera, collecting the data with 20 kV accelerating voltage and the probe current of 10nA at working distance up to 18 mm with 70° tilt angle. The post-processing analyses were done by TANGO-CHANNEL5 software. Scanning of the samples were detecting at a 300x magnification with 2 μm step size, providing a detected area of 910*680 μm². Due to the varied range of grain sizes, that step size was allocated by the average scale of fifth to tenth of the average grain size (AGS) while it was established for a fixed scale for all of the EBSD maps aimed at a comparative investigation.

3. Results and discussion

3.1. Magnetic behavior evaluation

The magnetic tests were applied for all CD and heat-treated (annealed) specimens. Likewise, Figs. 4 and 5 represented such obtained results of magnetic hysteresis loops for the minimum, median, and maximum values of the relative magnetic permeability (RMP) referring to all defined series of samples indicating differences in reduction rates, annealing temperature, and incubation time. Afterwards, EBSD analyses were implemented on the detected aforesaid samples. Another magnetic property, which was examined, was coercivity field or coercive force. The smaller coercive forces show the softer ferromagnetic materials and vice versa. Overall, the analyses specified
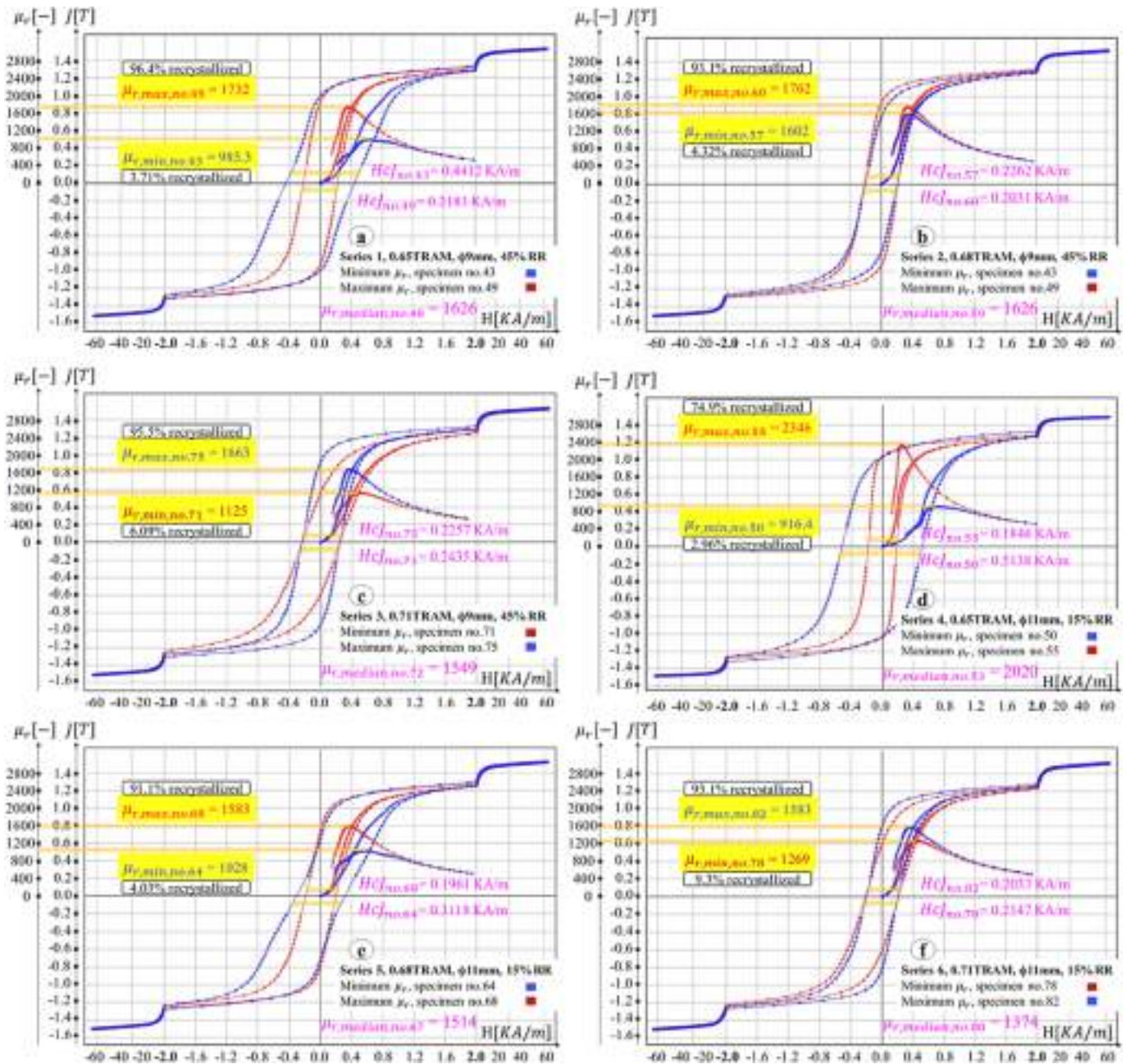
Fig. 5. The results of magnetic hysteresis loops for the annealed specimens, containing the materials with 45% RR under a) 0.65TRAM, b) 0.68TRAM, and c) 0.71TRAM besides that of with 15% RR under d) 0.65TRAM, e) 0.68TRAM, and f) 0.71TRAM.

that the annealed specimens were softer than CD materials owing to their much lower coercivity by narrower hysteresis loops along with much higher RMP. It is significant to be noticed that the values are basically close or even intersected to each other among the samples that is due to the variations in repetition tests. However, the results indicated that the average values of RMP and coercivity were 1900 ± 300 and 200 ± 20 A/m for the almost fully annealed samples, versus 370 ± 30 and 620 ± 40 A/m for CD specimens.

3.2. Crystallographic analysis

From microstructural and textural points of view, the morphology of CD (unheated as-received material) and newly-formed grains was investigated by advanced characterization technique of EBSD in terms of size and growth of the grains as well as their orientations and grain

boundaries. Likewise, the trend of deformed and recrystallized fractions was calculated by the EBSD post-processing analysis. In this regard, following the cross-section profile along the rolling direction, a radial strip analysis was also detected from the core region towards the edge area. In other words, the representations of the microstructural maps in three states, including the center, edge, and radial strip were studied out by EBSD. The most noteworthy indication is that the deformed bars must be scrutinized at first for providing enough information about the history of grains at initial conditions.

3.2.1. After industrial cold wire drawing

As for the CD specimens before the annealing heat treatment, there are basically lower stresses in the grains of core regions in compared to the grains on the edge areas which are imposed by larger deformations in-line with the longitudinal drawing force. The lower deformations in
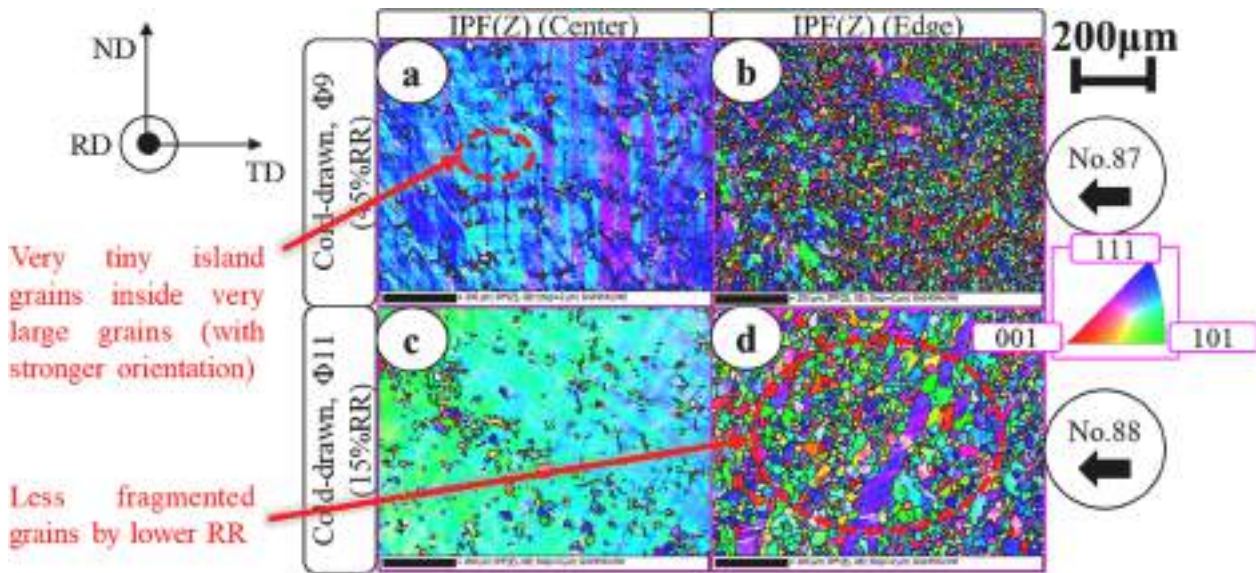
Fig. 6. IPF maps of unheated bars with two different RR a) in the core region of the specimen No.87 with 45% RR indicating tiny island-shaped grains inside very large grains, b) on the edge area of the same specimen, c) in the center of the sample No.88 with 15% RR showing less fragmented grains in compared to the higher RR, and d) on the edge section of the same sample.

the center provoked larger elongated grains following lesser fragmentation of the grains as shown in Fig. 6.

According to the inverse pole figure maps (IPF) in Fig. 6, the grains on the edge region had greater cold-strain-stretching deformation, resulting in comparatively more fragmentation of the grain, which formed under deformation-induced cold wire drawing. Overall and owing to Fig. 6 and what would be further elaborated in Fig. 7, in these CD FSS samples, higher RR evidently led to more elongated grains. The core region demonstrated longer and larger grains, while the edge proved shorter and narrower grains due to increased cold deformation and fragmentation. Consequently, the core exhibited small, island-shaped grains within those larger grains, as shown in Fig. 6a and c. This featured the influence of reduction rates on grain morphology. These IPF maps (Particularly IPF(Z)) illustrated the different crystallographic orientations through such color-scale image, encoded into the rolling direction (RD) on the plane of ND and TD. In addition, it was observable that the preference for textural tendency lie on ⟨1 1 1⟩ towards ⟨1 2 2⟩ and ⟨1 0 1⟩ more strongly in the core corresponding to the grains' elongation into the RD.

Fig. 7 depicted the microstructural radial strip map from edge to the center containing of the low and high-angle grain boundaries exactly compliance with the IPF maps. Any misorientation angle of a grain among the neighboring grains that was equal or higher than 15°, defining as θ > 15°, was defined by the high angle grain boundary (HAGB), while the low angle grain boundary (LAGB) was assigned by θ < 15°. To be precise, the misorientation angles from 2° to 15° were allocated by the subgrain fields, which is generating during recovery process. Furthermore, the grains which represented a misorientation angle of below 2°, from 2° to 15°, and above 15° were defined as the recrystallized, substructured, and deformed, respectively. It was proved that by increasing reduction rate from 15% to 45%, the spreading of LAGB increases all over the grains. The theory describes the intensity goes for the grains with in-grain shear bands attributable to the larger dislocation densities. Referring to the work by Bazri et al. [23] and Fig. 8, the complete landscape of elongated grains were discovered along the perpendicular views of ND/TD versus the cutting grains along the RD. While Fig. 8 illustrated such microstructures of FSS grade EN1.4105, the CD and annealed grains in EN1.4106 comparably displayed morphologies very similar to those observed in EN1.4105. This revealed the area of those of large primary grains, which can be

estimated in scale. In conclusion of this section, by increasing the reduction rate, the deformed grains would be evidently stretched more and more and reduced in their width until the fragmentation is occurring, and that is why longer, and larger grains are appearing in the core versus the shorter and narrower grains on the edge.

3.2.2. After recrystallization annealing

Even though some material properties such as mechanical hardness and strength are impressively improved by cold working processes, it is often necessary to return to original conditions by annealing, as implemented in this work. Three consecutive microstructural-based stages of recovery, recrystallization, and the grain growth are formed over the annealing heat treatment process, which will be discussed in this section. Recovery stage basically happens at low temperature scale while the following sequential structural modifications emerge. Referring to several literature such as the study by Kang and Yoon [24], while the point defects and clusters (aggregation of point defects) are undertaken by movement and elimination, the dislocation densities (DD), as the line defects, will be annihilated and rearranged as well. The subgrain formation, which involves the low-angle grain boundaries, are the next change in planar structures that is defined as polygonization. Lastly, the nucleation (recrystallization nuclei) is being formed that will be elaborated in detail with the kinetics of recrystallization.

Fig. 9 represented the EBSD-based maps of IPF(Z) and recrystallized grains for all defined series of the specimens under different annealing conditions, by assigning the soaking temperature and incubation time as well as their reduction rate values. The textural analyses would be complemented in the next sections. According to Fig. 9a to f, and through the observations of recrystallization initiation and completion, the recrystallization nuclei were mostly and theoretically formed at the preferred sites such as the original grain boundaries (GBs). To clarify, the suitable locations for nuclei formation are the GBs. This is highly due to the nonhomogeneous microstructures of the plastically-cold-drawn material. This phenomenon can be seen in Fig. 10, as a comparison between specimens 87 and 43, although neither the exact timing of nucleation's initiation for observing the subgrain formation nor the identical zone of all samples could not be achieved.

Back to Fig. 9, all consecutive and subsequent stages of recovery, recrystallization, and grain growth were expectedly occurred much faster by increasing AST. From Fig. 9a to f, as the soaking temperature
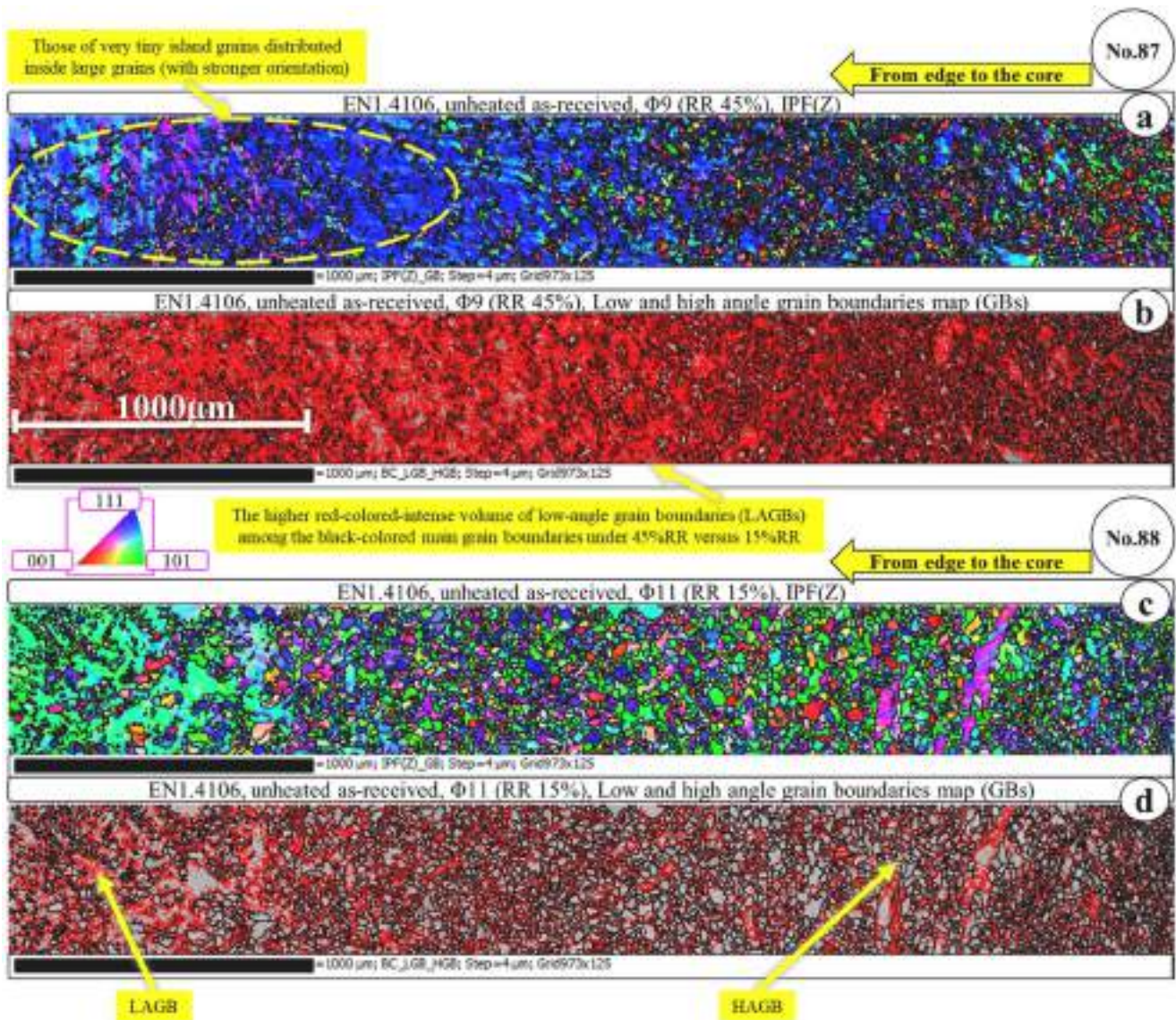
Fig. 7. The radial strip maps of CD round bar specimens before annealing with the reduction rates of 45% and 15%, including sample No.87: (a) IPF map, and (b) the LAGB & HAGB map as well as No.88: (c) IPF map, and (d) the LAGB & HAGB map.

and time increase, the more equiaxial and finer grains were progressively formed to consume all deformed grains over the recrystallization stage. Also, the significant effect of reduction rate played the same role as it also expectedly accelerated the recrystallization process. Subsequently, the migration of annealed GBs began, and larger grains were produced by the grain growth step, considering the growth in the average grain size (AGS). Ultimately, the initial expected stage of grain growth turned out to larger sizes than the initial grains (specifically this may have happened to the materials with higher RR); however, it is also risky to diminish the properties of the targeted material. It has been significant to be considered that despite reaching nearly complete recrystallization, (for some samples approximately 96% to 97% RF), the observed GBs have retained the curved morphology. The grain growth stage has been expected at the very beginning that may cause to generate further straight-shaped GBs through an advanced stage of grain growth. Moreover, considering the scale of the maps in Fig. 9 and all associated figures, while it was also expected that planar defects in boundaries would be enhanced during the recrystallization stage, a closer examination at higher magnifications such as 5KX to 10KX could reveal a more subtle evolution of GBs, showcasing variations in curvature in compared to the CD or incomplete recrystallizations. Although

recrystallization annealing is basically designed to eliminate crystalline defects and stabilize the material by reducing energy levels, the residual presence of defects after annealing cannot be still negligible with the impact on the material's overall integrity. Grain trend and growth would be completely discussed later in the next sections in this paper.

On the other hand, and according to Fig. 11, by increasing the annealing incubation time (AIT) from 5 min to 480 min, formation of HAGBs increased, and, conversely, the LAGBs disappeared in terms of boundary migration. This was notable to compare the maps with Fig. 7 (Sample No.87) as the unheated material. In this case, the subgrain domain and boundaries which were accompanying with the recovery of deformed grains transmitted to the recrystallized grains over the time. In fact, by reaching the critical value of DD, LAGBs transformed into HAGBs, causing the formation of new grains for occurrence of recrystallization. Also, the activation of dislocation movement accelerated the annihilation of dislocations. By such decrease in LAGB ratio, the average misorientation was also decreased. This is while the HAGBs which are favorable to enhance the mechanical behavior of the material show their determinative role from the CD to fully recrystallized samples.

Among all EBSD-based studied specimens, the minimum and maximum calculations for the grain sizes and recrystallization fractions
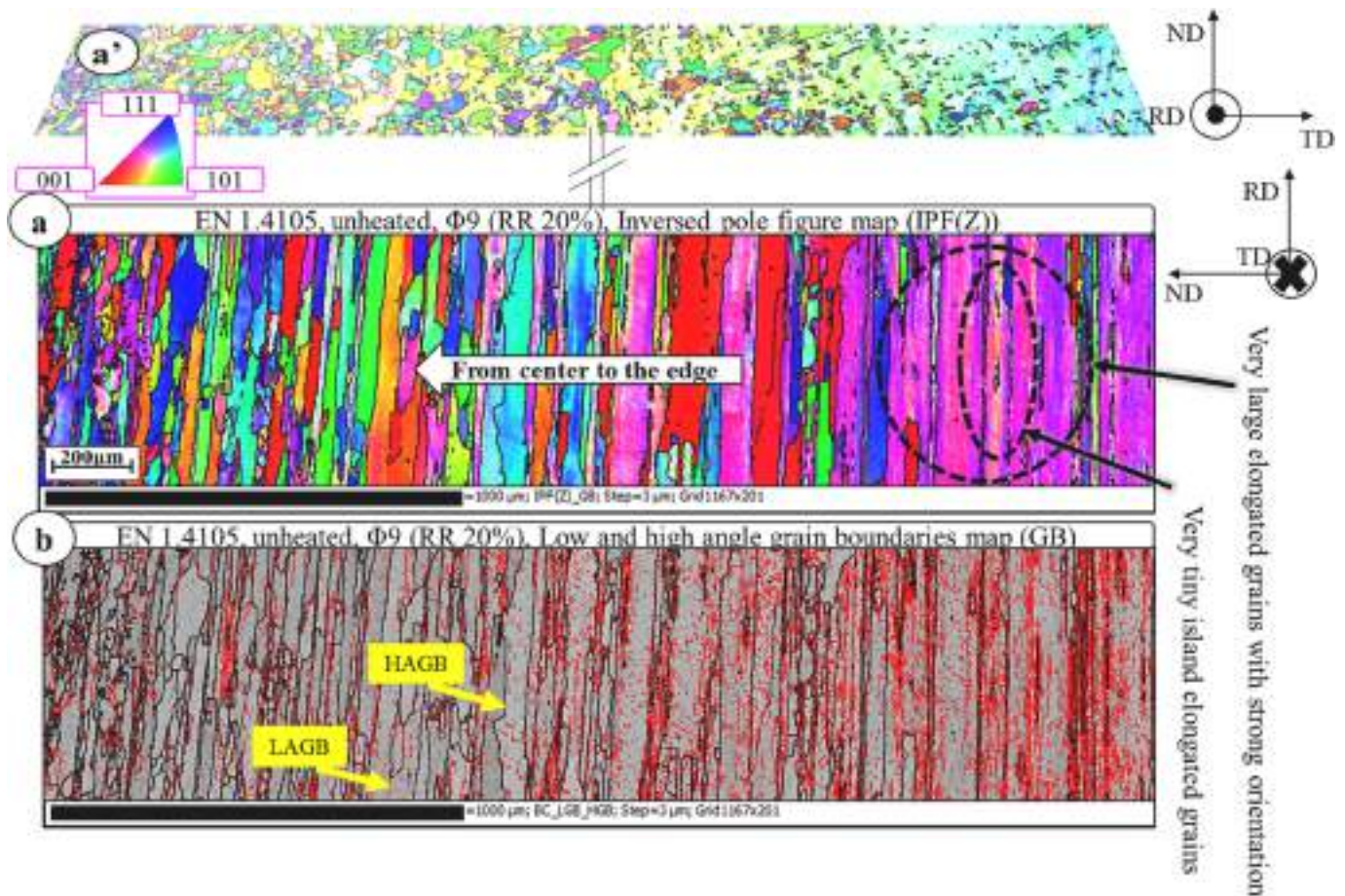
Fig. 8. The cross-section of a specimen along TD or ND of the EN1.4105 cold-drawn round bar with the 20% RR demonstrating the large elongated grains in terms of (a) IPF map and (b) the LAGB & HAGB map versus (a') the cross-section of the same sample along RD [23].

were revealed to compare with the unheated samples and for a better perception about the results. Samples numbering 43 and 49 under 5 min and 480 min AIT both with 0.65TRAM annealing soaking temperature (AST) for 45% RR specified the minimum and maximum of RF of 3.71% and 96.4%, respectively. In the same way, numbers 50 and 82 under 0.65TRAM of AST with 10 min AIT and 0.71TRAM of AST with 160 min AIT were also detected for 15% RR, respectively. Concerning the minimum and maximum of relative magnetic permeability (RMP), No.43 with the minimum RF has had the lowest RMP versus the maximum value for No.60 under 0.68TRAM of AST with 60 min AIT providing 93.1%RF for 45% RR. This indication went for specimens' numbers 50 and 55 under 0.65TRAM with 10 min and 320 min in case of 15% RR. Get-together it could be implied that the materials with minimum recrystallized newly-formed grains possessed minimum RMP.

3.2.3. Textural evolution

The textural tendency affects material behavior, including magnetic, mechanical, and corrosion resistance. Nevertheless, the relationship between reduction rate and the texture tendency can vary dependent on the history of microstructure, the processing condition, the chemical composition, and other factors. As it was observable, the IPF map shows the crystallographic orientations within all grains and their overall distributions respective to the reference coordination system. The higher recrystallization fractions lead to more diverse distribution of colored-code orientations compared to the deformed samples in the IPF maps since during the recrystallization the newly-formed grains were replaced by the deformed/strained grains. This was why they have had a wider range of textures (Fig. 12) which depends also on the nucleation sites, the grain growth, as well as the other local microstructural conditions, including the strain history, orientations of neighboring grains, and so on. This is while the higher recrystallization fractions tend to have more equiaxed grains in comparison with the deformed or incomplete recrystallized grains. Consequently, the higher recrystallized grains exhibit a range of orientations, depicting a distribution of colored-code orientations. In addition, it is perceptible that for the CD samples the textural preference contributed to $\langle 111 \rangle$ towards $\langle 122 \rangle$ and $\langle 101 \rangle$ specifically in the center corresponding to the grains' elongation into the RD while the annealed samples did not specify a strong tendency that is also compatible with PF outputs. In this regard, the tendency of the grains for the textural orientation could be more understandable from Fig. 12 which showed a stereographic projection from cube to sphere in conjunction with IPF triangle map.

In terms of textural analysis, the graphical pole figure (PF) map also assisted to analyze the crystallographic planes. Fig. 13 represented the PF maps, which plot the colored-contour scale of intensity or density of crystallographic family planes (as for the symmetric clusters that form around certain lines or points) as a function of the sample orientation by using the stereographic projection as the post-processing EBSD analyses. The direction of the poles on these plane PFs specified the orientation or texture of the planes in the material. The concentration of poles implied the fraction of grains with a particular orientation. Therefore, the dense clusters of poles showed a preferred orientation whereas the more uniform distributions suggested a random orientation. Moreover, the center point (pole) of these maps characterized the direction perpendicular to the specimen's surface while the outer edges addressed directions parallel to the surface.

Fig. 13 displayed the plane PF maps of {1 0 0}, {1 1 0}, and {1 1 1} for the specimens of CD material with 45% RR alongside 0.65TRAM with 5

min and 480 min AIT of the same-source CD material as well as the CD condition with 15% RR plus 0.65TRAM with 10 min and 320 min AIT from the initial unheated sample. For measuring the degree of preferred orientation or alignment, the misorientation uniformity distribution/density (MUD) parameter was used to represent the deviation from a random or uniform distribution of crystallographic orientations. The outputs were used after normalizing the contour scale delineating the MUD. The strongest texture arisen form the unheated samples is the (1 0 0) plane family with almost maximum comparative MUD, that displays the more intense clusters through the series of specimens addressing the rolling direction. Indeed, even after the recrystallization, the observation of a sort of preferred textural orientation is normal since the recrystallization itself causes to develop new grains with specific crystallographic orientations. This is true that the MUD values diminish after recrystallization in compared to the deformed state, however, it cannot obviously reach zero. Smaller deviations from the entirely random orientation distribution can be expected owing to the factors such as history of cold working, nucleation site preference, grain growth and so on.

While it is observable that more clusters but with lower MUD values for higher recrystallized samples appear compared to the cold drawn deformed samples with denser and lesser clusters, it implies that the higher recrystallized samples have more well-defined textures. The presence of more clusters points out the higher concentration of preferred crystallographic orientations or families of planes. On the other hand, the lower MUD values for the higher recrystallized samples prove the higher degree of textural uniformity or alignment. These findings are consistent and in agreement with the understanding that recrystallized materials tend to develop more organized texture compared to deformed materials.

Fig. 14 represented the ODF sections, which were processed before and after annealing. ODF maps, *f(g)*, were computed by correlating each orientation of $g = \{\varphi1, \Phi, \varphi2\}$ considering Gauss-based approach with a half-scattered width of $\psi0 = 2°$ in the Euler space. To this end, these FSS CD samples are consisted of the α-fibre texture close to the typical direction of ⟨110⟩, and more specifically to {223} ⟨110⟩ and {111} ⟨110⟩, which is (111)[1$\bar{1}$0], orientation. In addition, higher intensity can be seen in higher reduction rate. For the annealed specimens, the texture distribution along the γ-fibre were also more strongly observable owing to the incomplete and progressive recrystallisation while by increasing the AST and AIT, the orientations along the γ-fibre were formed gradually with more tendency to {111} ⟨011⟩, which is (111)[0$\bar{1}$1], orientation. In this regard, Fig. 6 illustrated the ODF contour-lined maps in
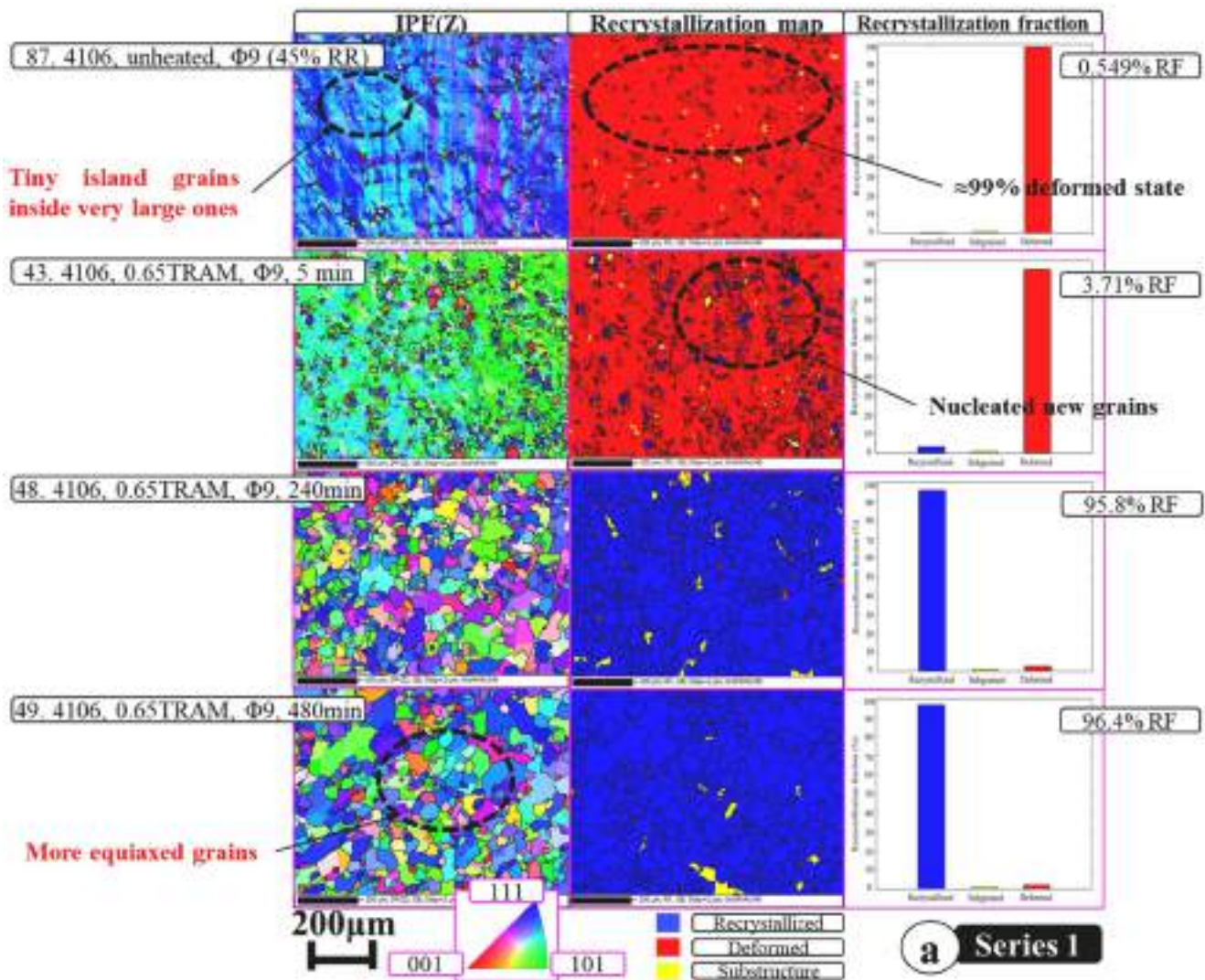

Fig. 9. EBSD-based output, including IPF(Z) and recrystallization maps, for all 6 defined series of the specimens under different annealing conditions, consist of a) 0.65TRAM, φ9 mm, 45% RR, b) 0.68TRAM, φ9 mm, 45% RR, c) 0.71TRAM, φ9 mm, 45% RR, d) 0.65TRAM, φ11 mm, 15% RR, e) 0.68TRAM, φ11 mm, 15% RR, and f) 0.71TRAM, φ11 mm, 15% RR.
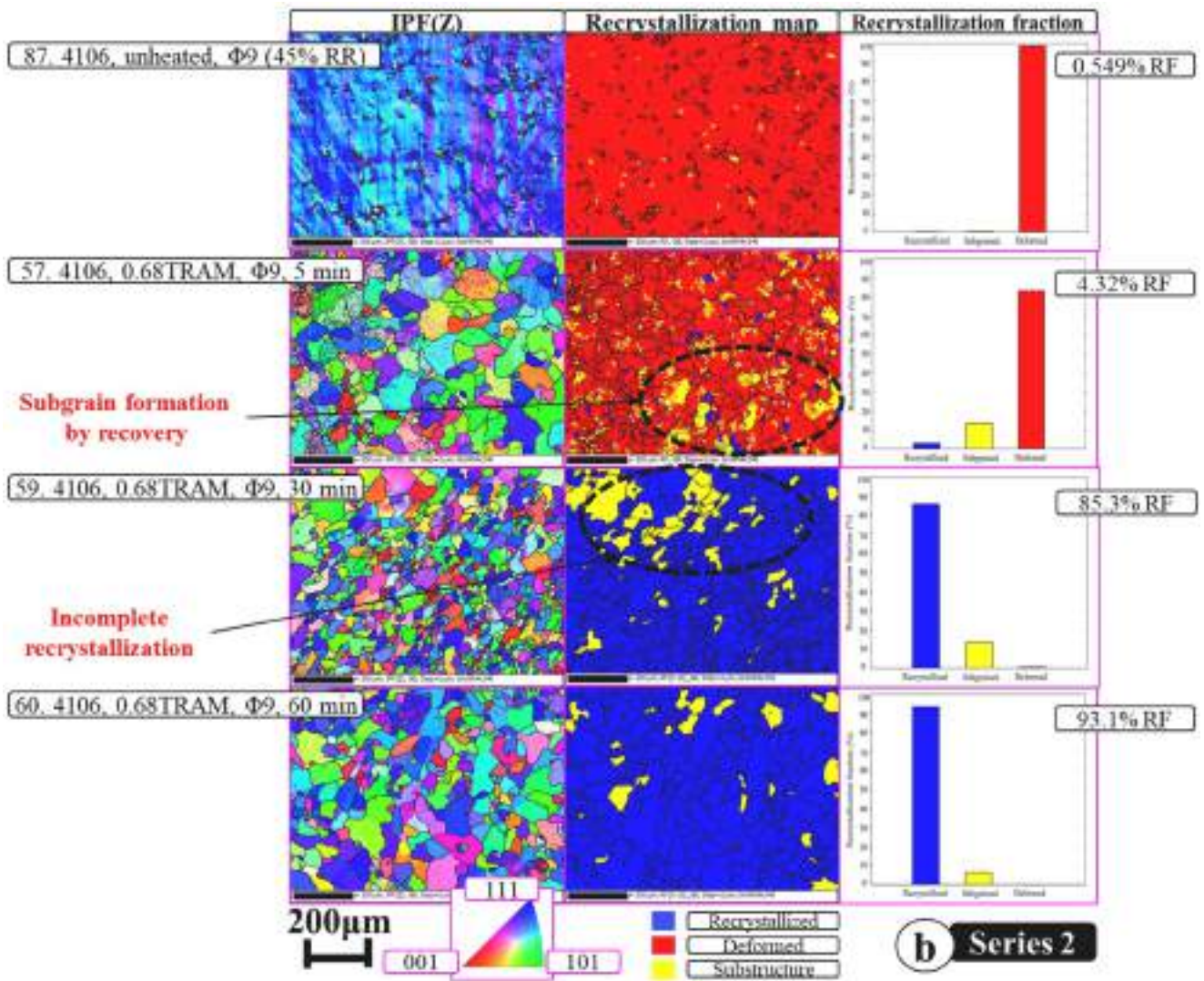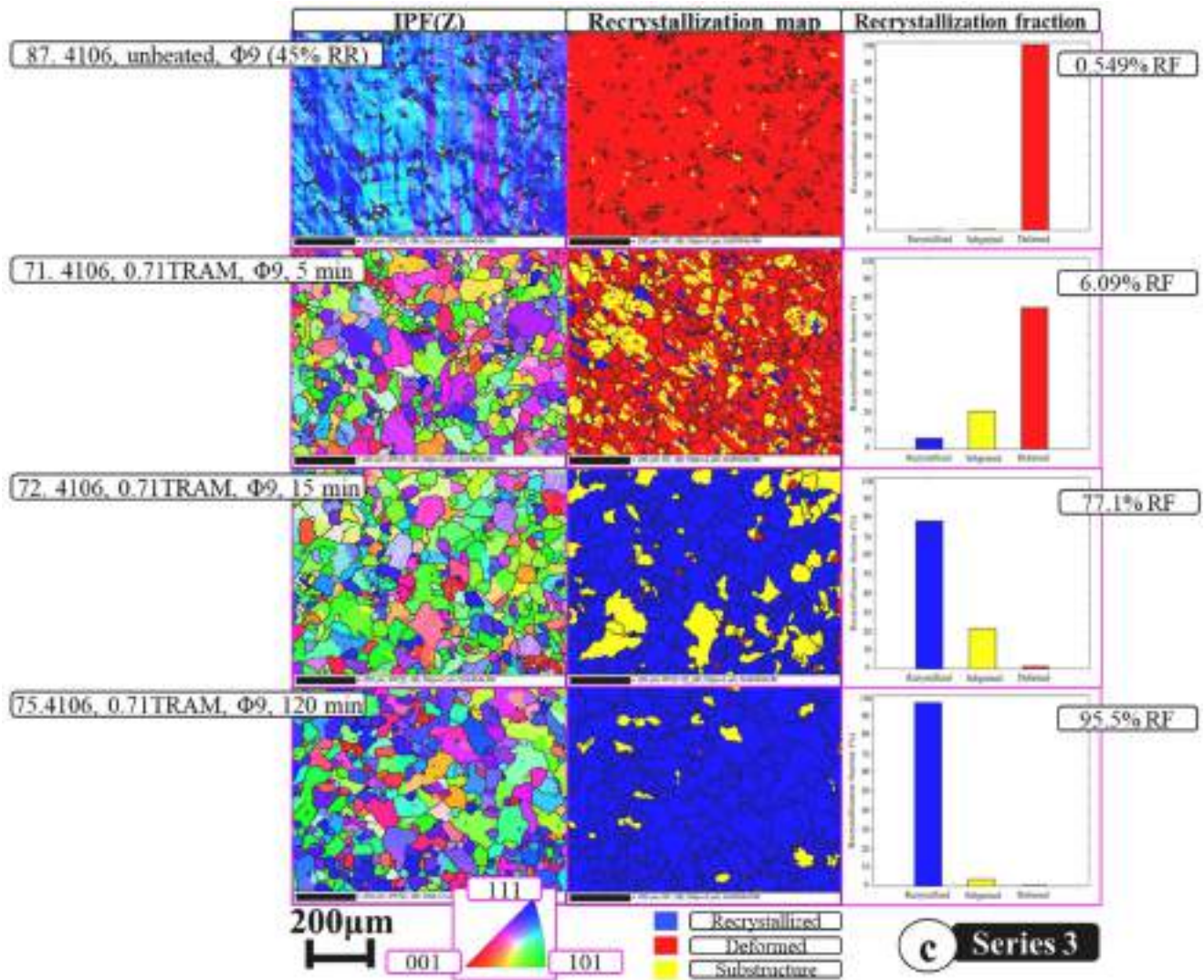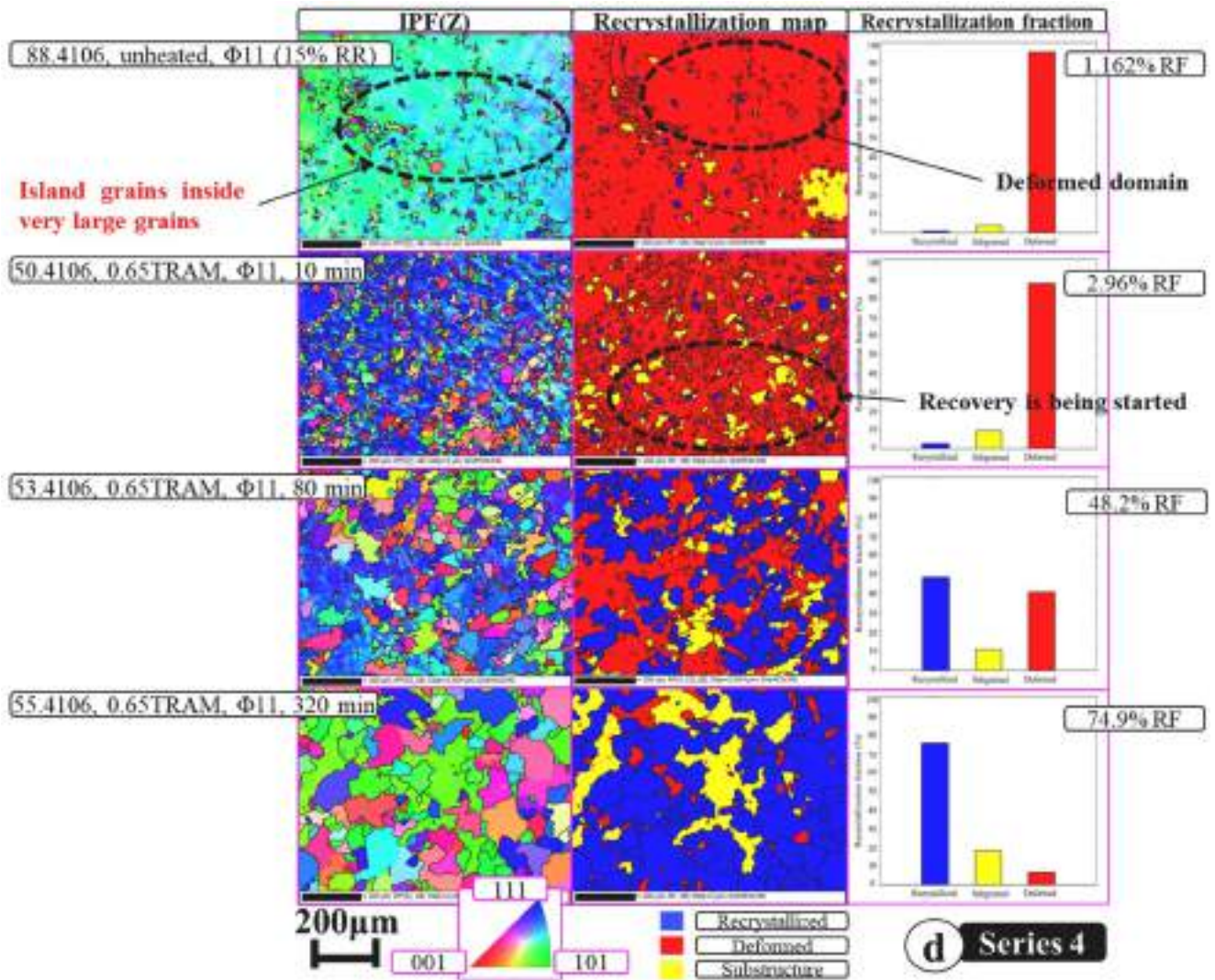
Fig. 9. (*continued*).

Fig. 9. (*continued*).

Fig. 9. (*continued*).

Fig. 9. (*continued*).

Fig. 9. (*continued*).

3.2.4. Grain growth analysis
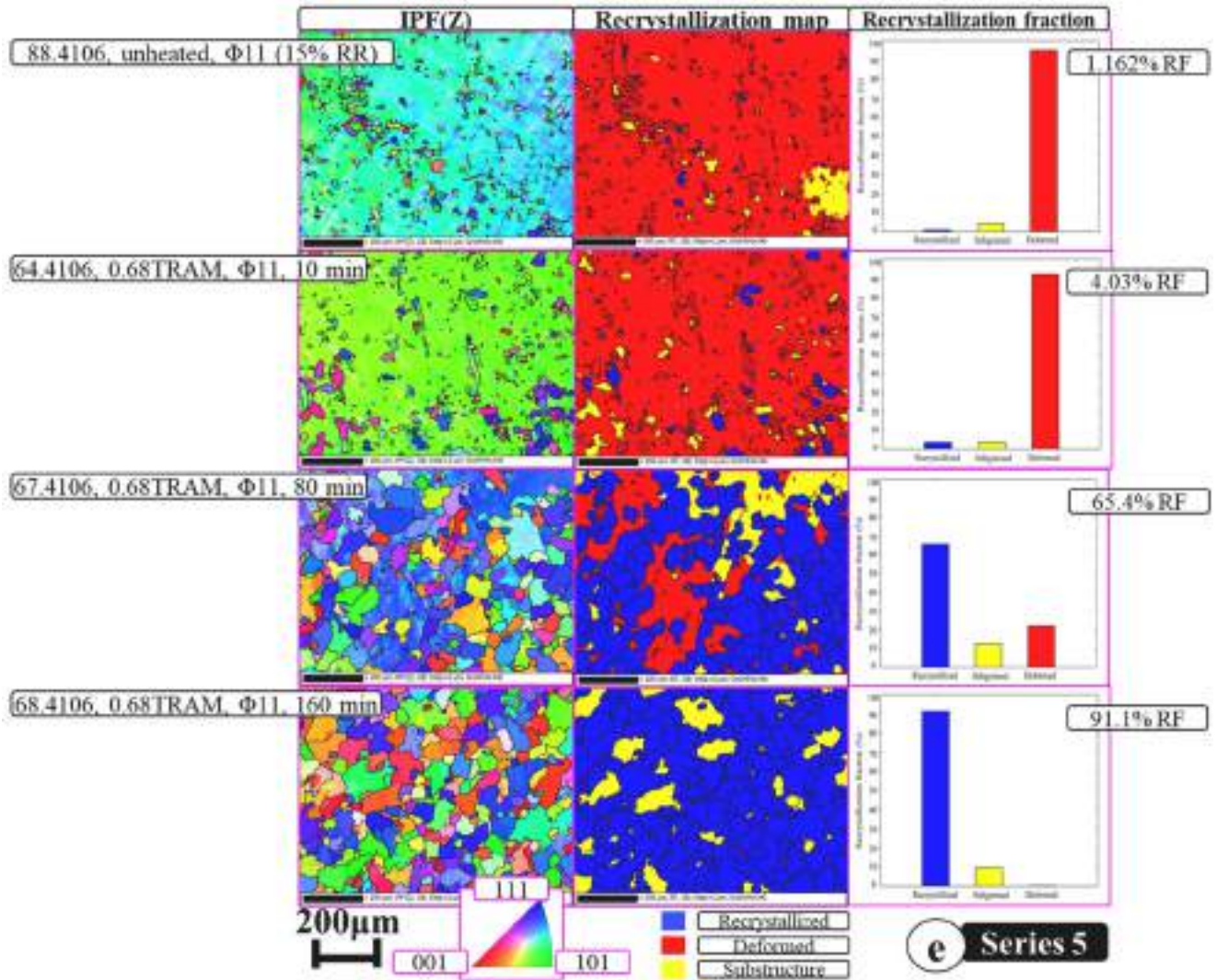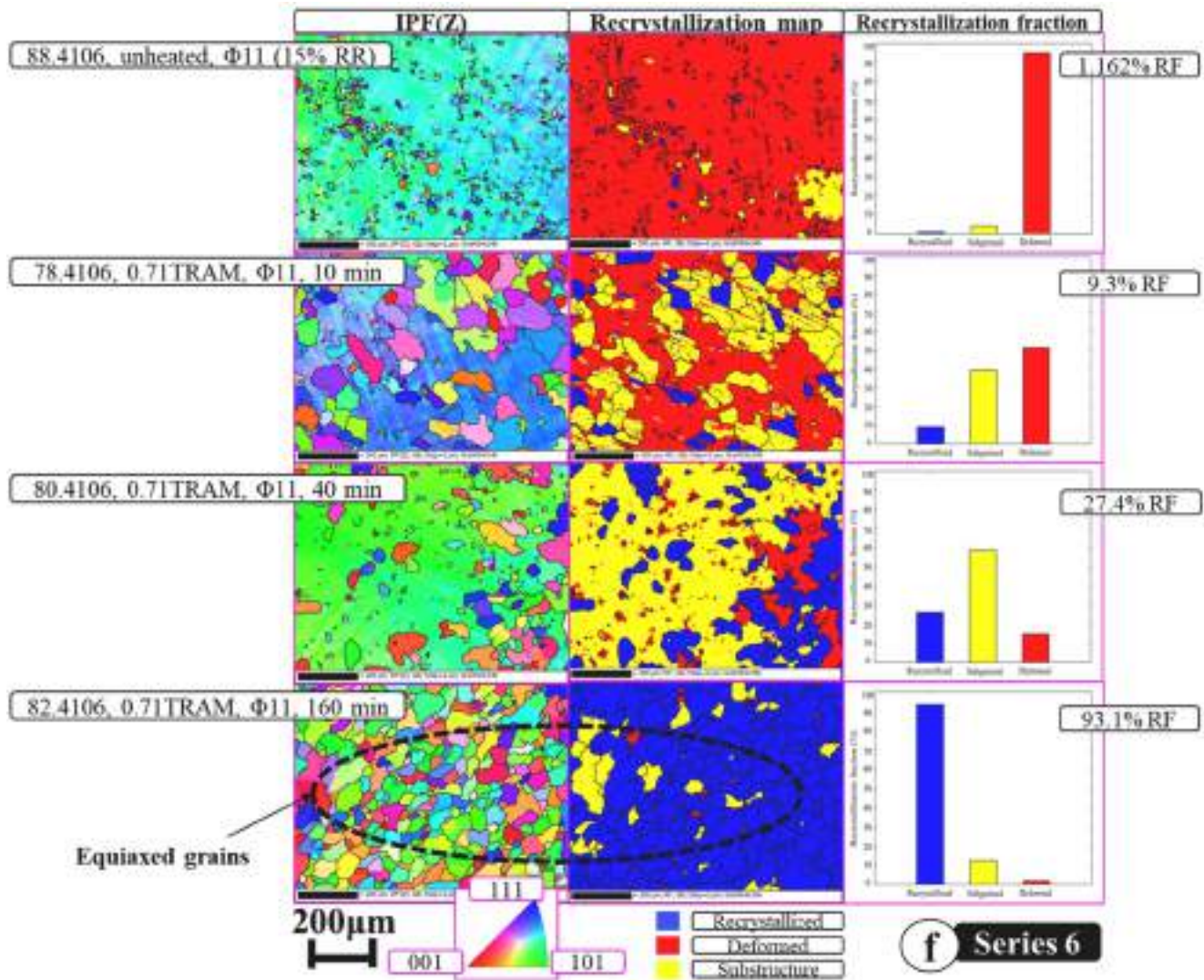
the sections of $\Phi 2$ from $0°$ to $90°$. The developed typical γ-fiber in such a recrystallized texture can be better understandable. Moreover, with higher recrystallization, the textures were become more distributed with less intensity compared to the CD samples or incomplete recrystallization.

3.2.4. Grain growth analysis

Next, it is going to analyze the grain-size trend and the probable growth mechanism. Apart from the EBSD analyses, by using the liner intercept method referred to ISO 643 (Steels, micrographic determination of the apparent grain size) and ASTM E112 (Standard test methods for determining average grain size) on OM images [25], the AGS were measured before and after annealing. The reason was due to the limited possibility of costly EBSD method to detect all the samples for drawing the grains' graph. Fig. 15 showed that it was metallurgically obvious that the AGS generally increased by increasing AST and AIT, while it conversely decreased by increasing RR.

In addition, Fig. 15 illustrated that how the trend of AGS from the CD unheated materials, with subsequent recovery, partial and full-recrystallized grains, as well as the grain growth shaped. The results showed that the overall wide-ranging AGS were from 45.44 μm to 46 μm for 45% RR and from 58.24 μm to 52 μm for 15% RR in the center of the samples. It is noteworthy that higher RR caused smaller grains owing to the more deformed and fragmented initial grains. Moreover, the results demonstrated that the applied annealing incubation time has not lasted enough to reach the grain growth step for having larger grains than the original ones. However, this was also related to the behavior of this FSS grade whereas the other study by [23] reported the grain growth formation in case of another grade of EN1.4105 within very much defined similar annealing procedure. The largest sizes of newly-formed grains happened at 0.71TRAM with maximum applied AIT, and the lowest values, apart from the CD samples, belonged to 0.65TRAM with minimum AIT. Moreover, the three least heat-treated samples of numbering 43 arose from CD No.87 as well as No.50 and No.64 from CD No.88 depicted the landscape which had such a tiny island-shaped grains with the largest AGSs after CD materials.

3.2.5. Recrystallization kinetics

As for analysis of the recrystallization kinetics, equation (14) is obtained by using the fundamental JMAK model. By using the achieved data from the experiments and EBSD-based postprocessing analysis, the JAMK curves were plotted, as shown in Fig. 16. Fig. 16a illustrated the curves for each of the defined series. The JMAK exponential power of *n* constant for all series of annealing conditions were calculated by employing the equation (14) (Fig. 16b). Nevertheless, this value can be computed by the curves of JMAK kinetics following Fig. 16d.
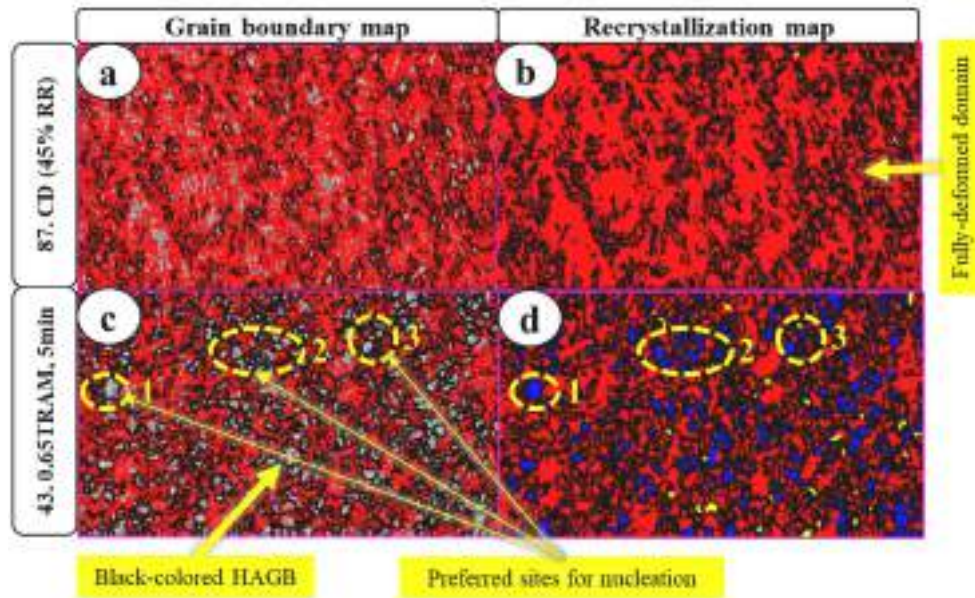
Fig. 10. EBSD-based overview track of the recrystallized nuclei following the preferred sites of the original CD grain boundaries: a) GBs in the CD sample, b) recrystallization map of the same detection, c) the GB of the newly-formed recrystallized nuclei in the specimen under 0.65TRAM within 5 min incubation time, and d) the recrystallization map of the same domain, (preferred sites of 1 to 3 for nucleation, corresponding to both maps).

$$\ln[-\ln(1 - X)] = n(lnt) + lnk \qquad (14)$$

Fig. 16c demonstrated the JMAK-modelled curves juxtaposed with the determination coefficient R^2 in the concept of linear regression to fit a linear model to the curves plotted. It assisted to evaluate how well such linear model represented the variations in the data. In addition, for better comparative interpretation Fig. 16d with the logarithmic state provided the exact findings of nucleation onsets and recrystallization processes with resulting microstructures. The recrystallization kinetics can be influenced by several indicators, including the stored energy or strain energy due to the CD deformation in terms of the driving force, the AST, the elemental composition, and other factors such as processing history of the material. The recrystallization rate is defined by the nucleation rate of new grains as well as the rate at which the new grains may grow.

By this experimental-based modelling for prediction of the rates of nucleation's in each series of material involved with studying the effect of cold working, the grains' nucleation were initiated after around 2, 2:30, and 2:30 min for 0.71TRAM, 0.68TRAM, and 0.65TRAM for 45% RR, respectively, whereas these initiations were approximately 3, 6, and 9 min for 0.71TRAM, 0.68TRAM, and 0.65TRAM for 15% RR, respectively as well. In other words, it is clear that the specimens annealed at 0.71TRAM for 35% RR exemplified the fastest recrystallization fraction owing to its earlier nucleation initiation. This trend drops down as the AST decreases. These results revealed that the sooner nucleation of recrystallization following the faster RF were induced by higher RR. Higher AST was also directly effectual in the same way. As it can be observable in Fig. 16d, the closest timing of EBSD prior analysis has been matched up by the specimen under 0.65TRAM and 10 min AIT for 15% RR in which the nucleation has been calculated by 9 min. In general, this study proved that the JMAK's exponential power was in the range of 1.58 to 2.50 outlining two-dimensional (2D) nucleation and growth of grain. Though such *n* values were in lower range than the expected plausible three dimensional (3D) growth, this variation has been also pointed out by fundamental studies such as [26] and [27]. It is also evident that the JMAK kinetic is temperature-dependent while the AST temperature increases, the exponent power of *n* decreases.

Going through more details, referring to the EBSD-based analyses and outputs of JMAK modelling, the maximum RFs for 45% RR, were detected by 96.4% under 0.65TRAM after 480 min with AGS of 35.37 μm versus the faster RF of 95.5% under 0.71TRAM only after 120 min with finer AGS of 41.21 μm. In this case, the lower RR of 15% exhibited the maximum RF of 93.1% again under 0.71TRAM after 160 min with 45.98 μm. During very beginning of ISRAHT and after the nucleation stage, the recrystallization fractions is harshly increased by increasing of AST. The trend of recrystallized formation is perceptibly increased by the higher temperature and time of annealing. Later on towards the higher percentage of recrystallization, such drastic ascending behavior of exponential-oriented kinetic curves continues with a smoother move. On the other hand, the significant effect of reduction rate arisen from the preceding CD process is in direct proportion with recrystallization progress. This output validates that the recrystallization fractions increase with increasing the CD RR. For example, the computed curves illustrated that the RF were around 4%, 8%, and 12% over 20 min of AIT for 0.65, 0.68, and 0.71TRAM of 15% RR, respectively. These amounts followed by 41%, 58%, and 96% for 45% RR, respectively. Overall, as a result, the microstructural analyses of these heat-treated materials demonstrate that the recrystallization kinetics has been in good agreement with the JMAK theory.

In the current research, several above-mentioned properties, including the thermophysical properties, (e.g., temperature, and melting point), the mechanical properties (e.g., the cold-worked deformation, and consequent reduction rate), as well as the tribo-metallurgical properties, comprising of microstructural and textural characteristics would affect the stored energy and the primary stage of recrystallization. From comparative point of view, by increasing the cold drawing percentage, which causes smaller and more fragmented grains, the AST can be adjusted to decrease for the same fraction of recrystallization at lower cold-worked condition that can be seen also in Fig. 16. In addition, the overall sizes of grains for 45% RR were smaller than that of 15% RR. On the other hand, the cooling stage is influential to the recrystallization formation. To clarify, rapid cooling process can lead to form abundant nucleation sites and smaller new-formed grains, whereas SCP leads for forming fewer nucleation sites in conjunction with growth of fewer and purer crystals, even though it would plainly allow the grains for becoming larger. As a result, slower cooling has been preferable in this study that was compatible for the targeted non-hardenable FSS.
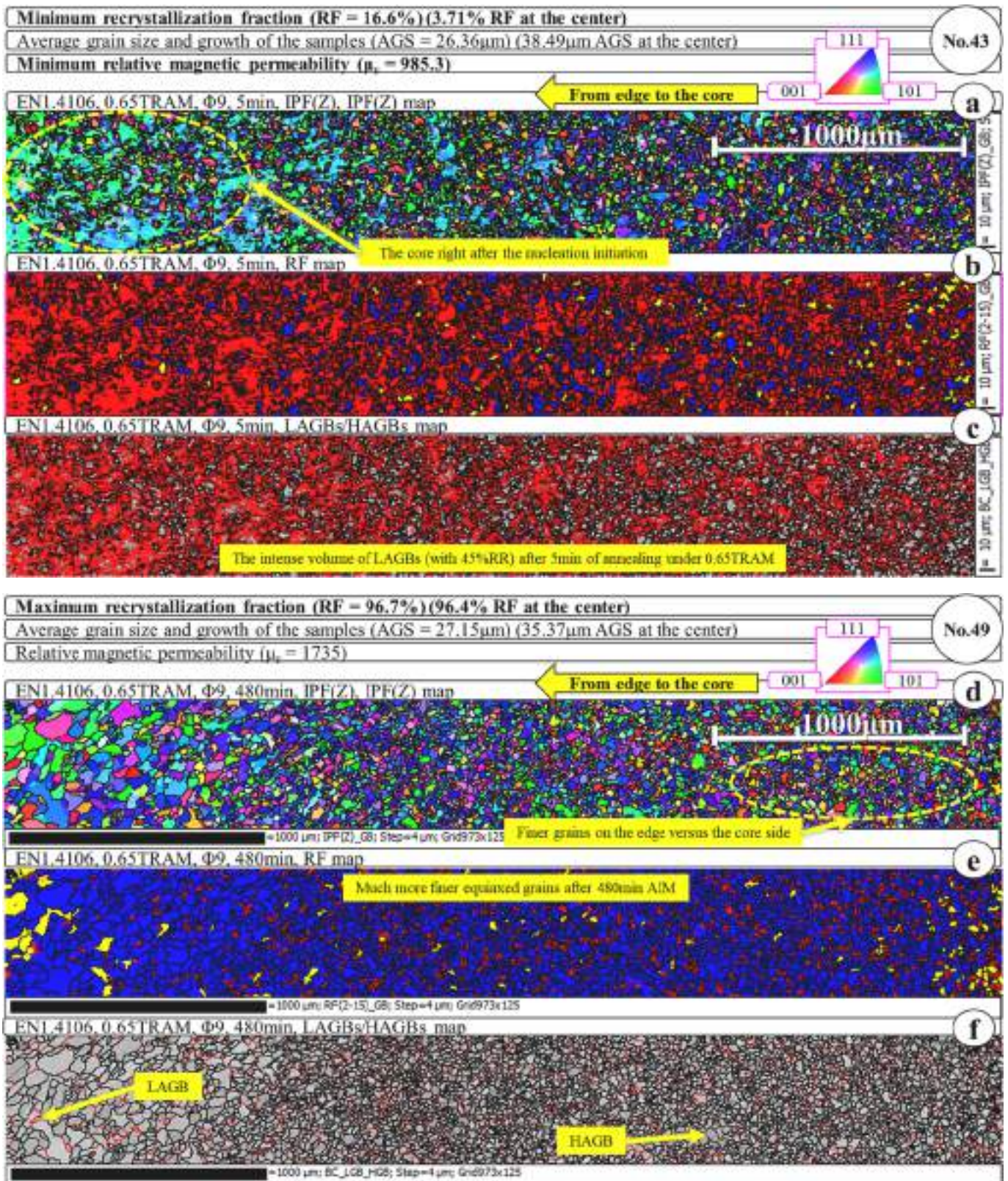
Fig. 11. The radial-strip maps (from edge to the center) a) IPF(Z), b) RF, and c) LAGBs and HAGBs for sample No.43 under 0.65TRAM of AST with 5 min AIT signified the minimum RF as well as d) IPF(Z), e) RF, and f) LAGBs and HAGBs for sample No.49 under 0.65TRAM of AST with 480 min AIT showed the maximum RF among the specimens with 45% RR.
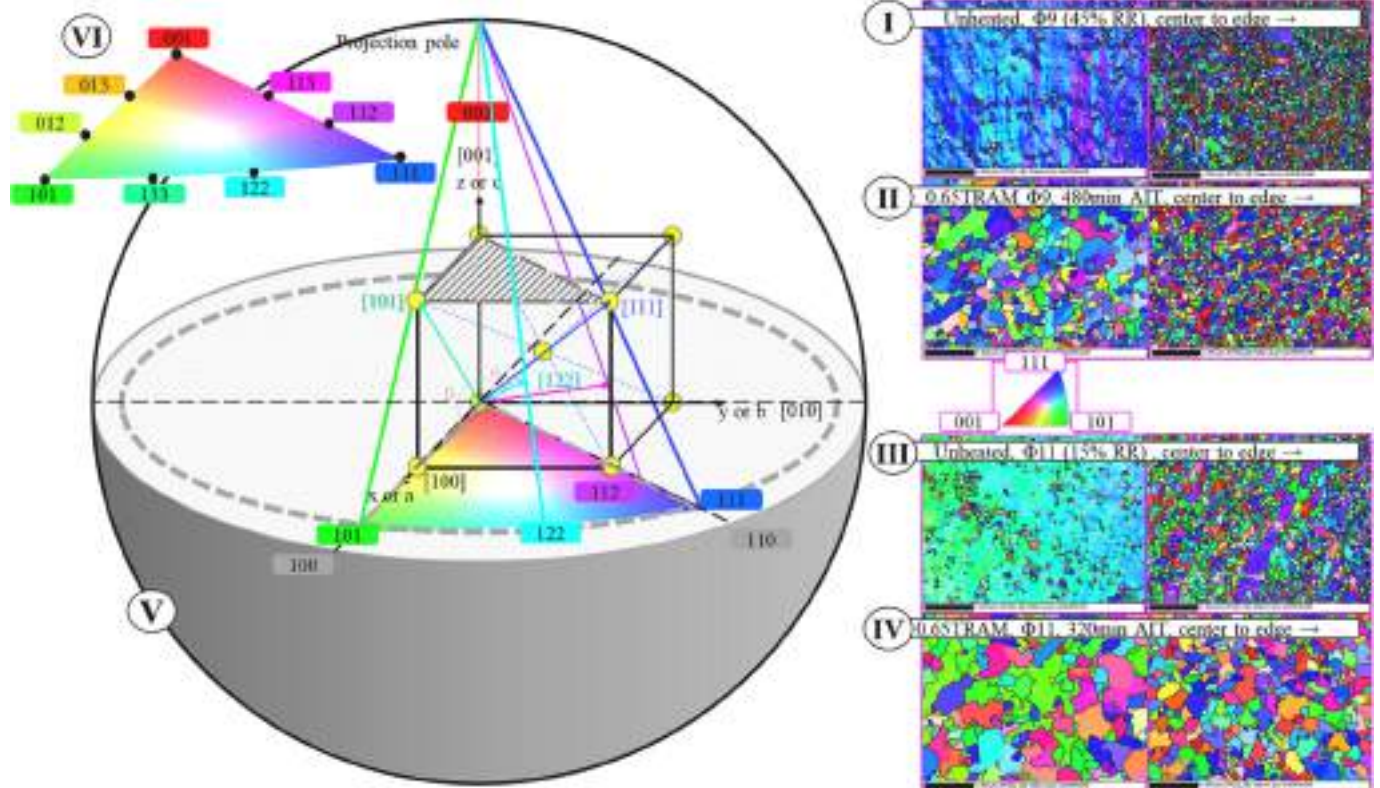
Fig. 12. Comparative observation among unheated and well-heat-treated specimens with different reduction rates (I to IV) owing to their textural orientations according to the stereographic projection for the 3D cubic crystal (V) in accordance with the IPF triangle (VI), including some examples of directions.
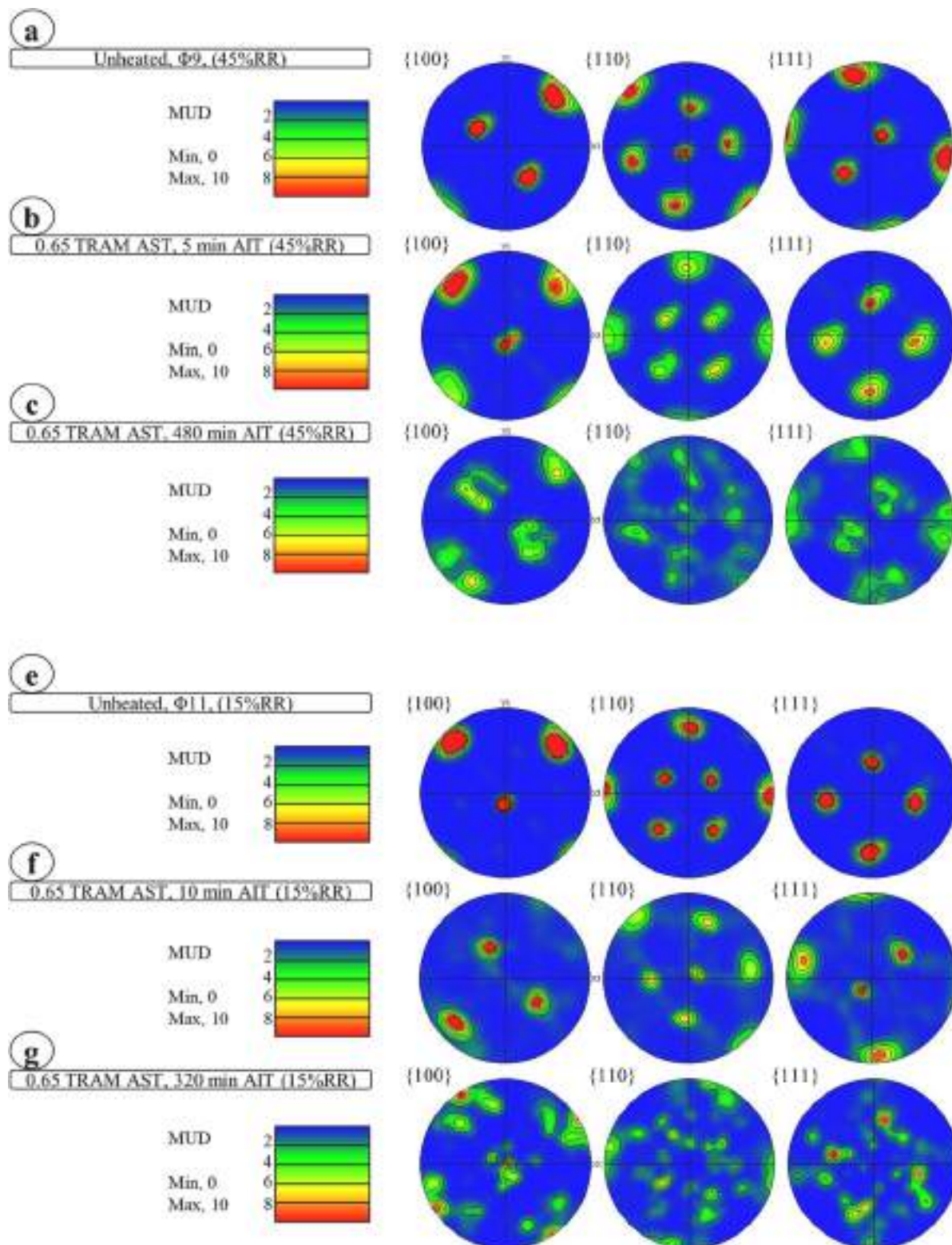
Fig. 13. Pole figure maps of the plane families of {1 0 0}, {1 1 0}, and {1 1 1}: a) CD with 45% RR, b) 0.65TRAM, 5 min AIT with 45% RR, c) 0.65TRAM, 480 min AIT with 45% RR, d) CD with 15% RR, e) 0.65TRAM, 10 min AIT with 15% RR, and f) 0.65TRAM, 320 min AIT with 15% RR, demonstrating the alignment of {1 0 0} parallel with the rolling direction.
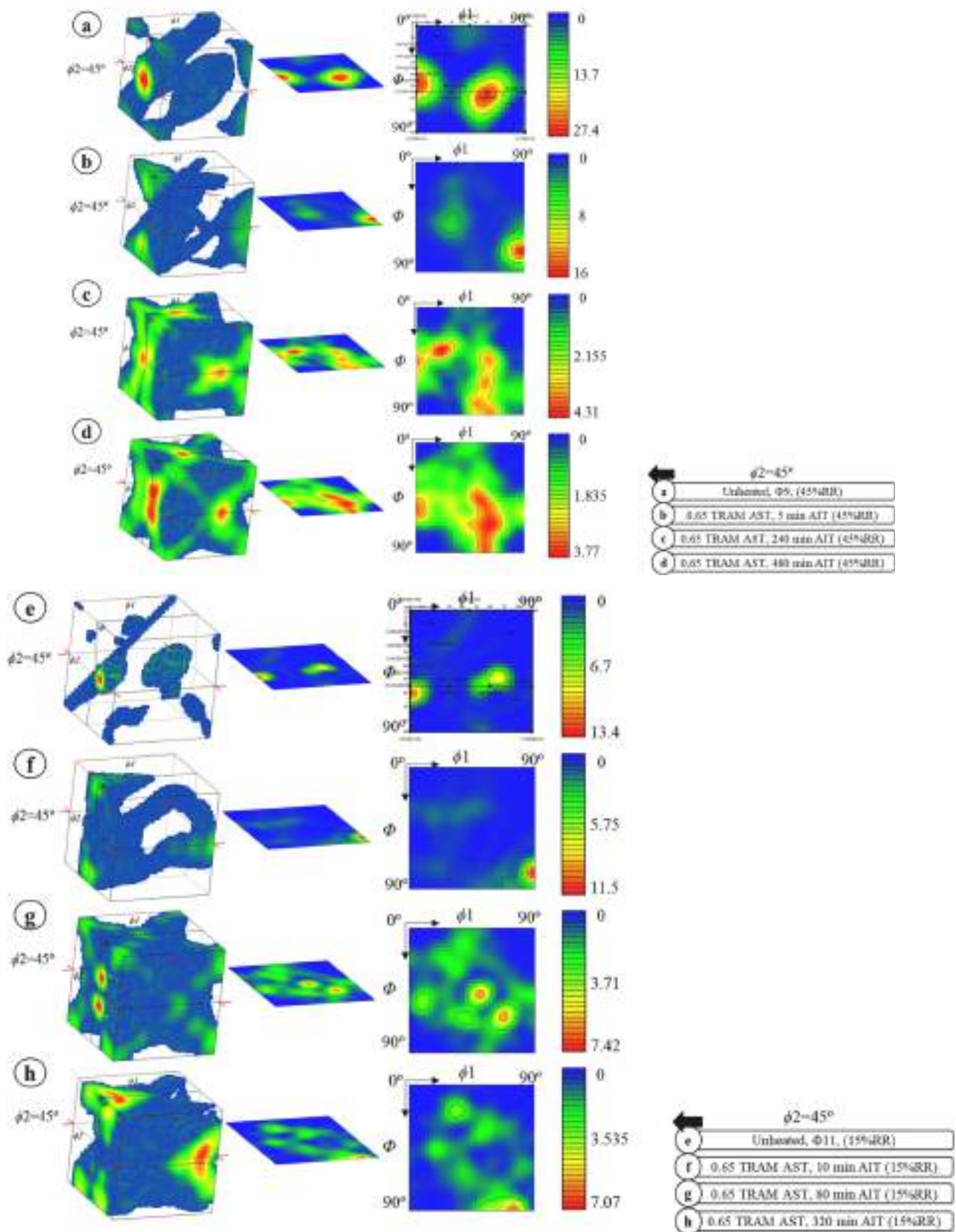
Fig. 14. ODF 3D scattered plots and maps, at $\phi2 = 45°$, of the a) CD with 45% RR, b) 0.65TRAM, 5 min AIT with 45% RR, c) 0.65TRAM, 240 min AIT with 45% RR, d) 0.65TRAM, 480 min AIT with 45% RR, e) CD with 15% RR, f) 0.65TRAM, 10 min AIT with 15% RR, h) 0.65TRAM, 80 min AIT with 15% RR, and h) 0.65TRAM, 320 min AIT with 15% RR, i) the sectional view of orientation distribution in almost fully recrystallized specimen of 0.65TRAM, 480 min AIT with 45% RR, j) important ideal positions of the interrelated texture components of BCC at $\phi2 = 45°$ section of the Euler space.
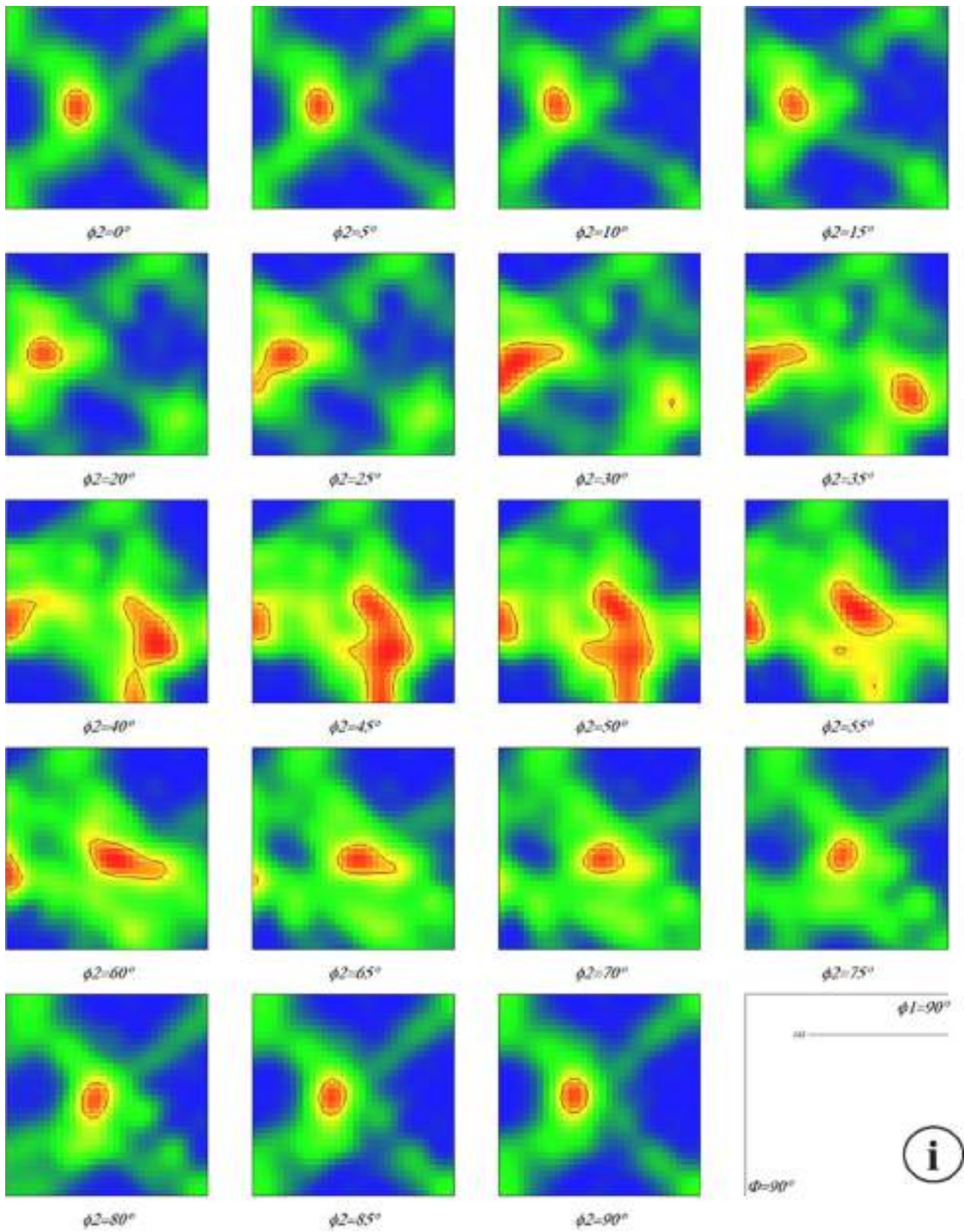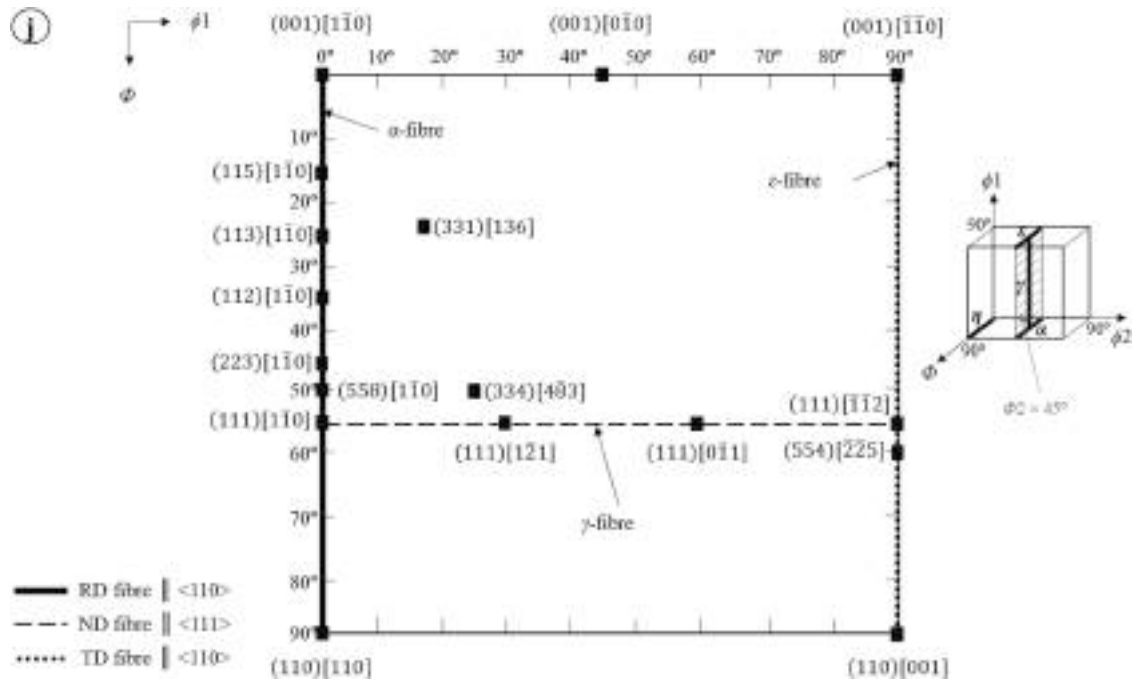
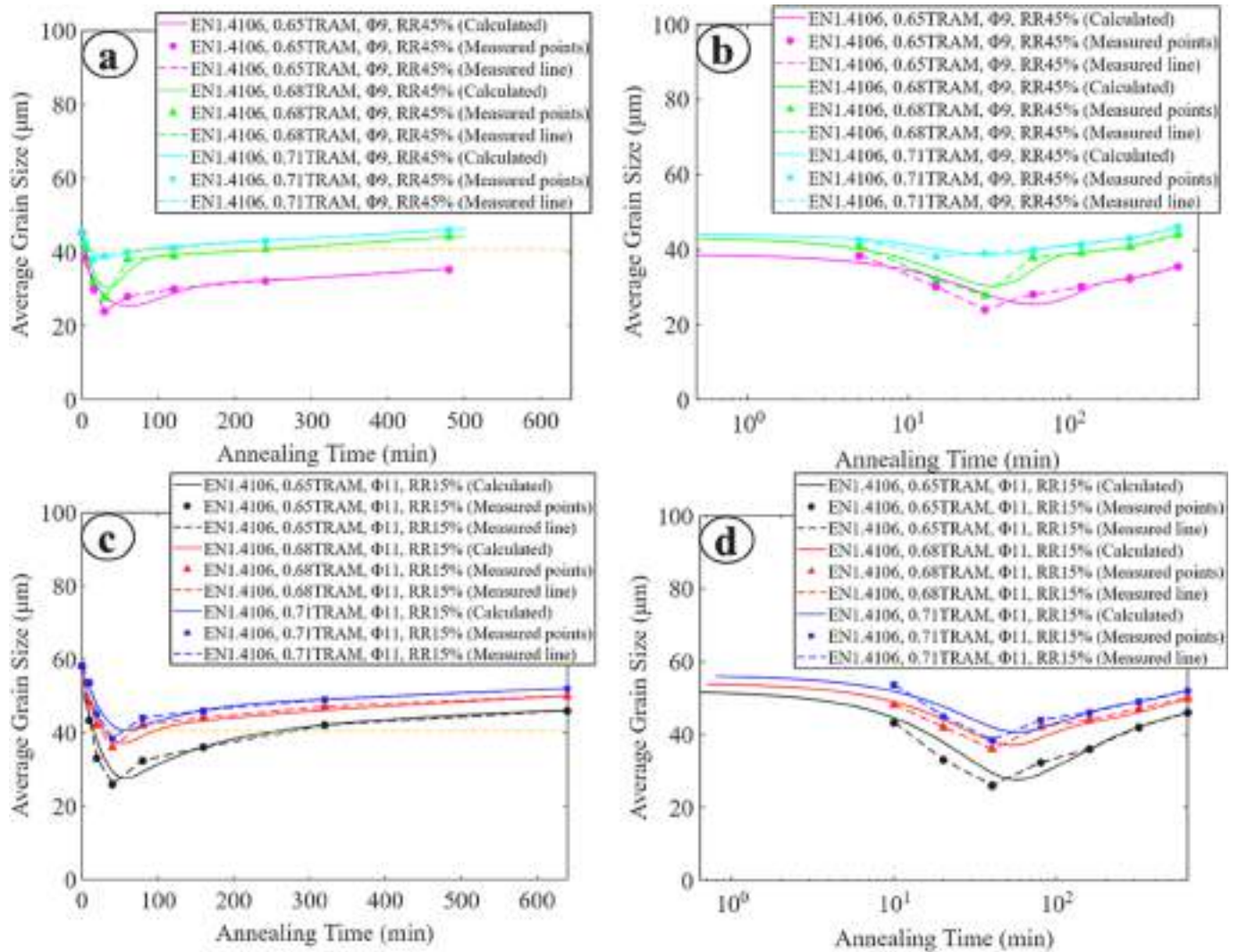**Fig. 14.** (*continued*).

Fig. 14. (*continued*).

Fig. 15. The trend of the AGS versus the AIT involving different AST for a) OM-based measurements for 45% RR, b) logarithmic OM-based measurements for 45% RR, c) OM-based measurements for 15% RR, and d) logarithmic OM-based measurements for 15% RR.
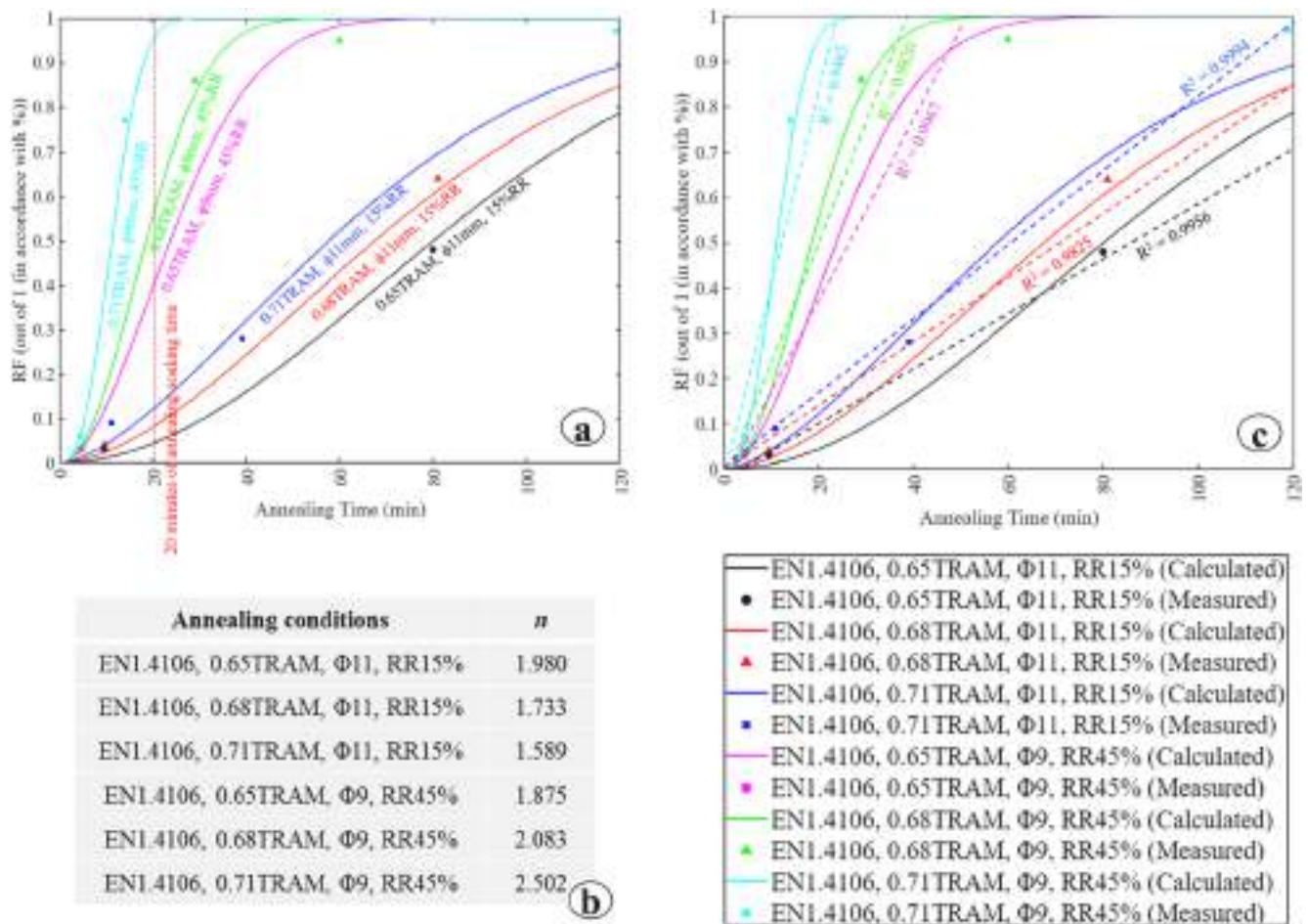
Annealing conditions	n
EN1.4106, 0.65TRAM, Φ11, RR15%	1.980
EN1.4106, 0.68TRAM, Φ11, RR15%	1.733
EN1.4106, 0.71TRAM, Φ11, RR15%	1.589
EN1.4106, 0.65TRAM, Φ9, RR45%	1.875
EN1.4106, 0.68TRAM, Φ9, RR45%	2.083
EN1.4106, 0.71TRAM, Φ9, RR45%	2.502

Legend:
- EN1.4106, 0.65TRAM, Φ11, RR15% (Calculated)
- EN1.4106, 0.65TRAM, Φ11, RR15% (Measured)
- EN1.4106, 0.68TRAM, Φ11, RR15% (Calculated)
- EN1.4106, 0.68TRAM, Φ11, RR15% (Measured)
- EN1.4106, 0.71TRAM, Φ11, RR15% (Calculated)
- EN1.4106, 0.71TRAM, Φ11, RR15% (Measured)
- EN1.4106, 0.65TRAM, Φ9, RR45% (Calculated)
- EN1.4106, 0.65TRAM, Φ9, RR45% (Measured)
- EN1.4106, 0.68TRAM, Φ9, RR45% (Calculated)
- EN1.4106, 0.68TRAM, Φ9, RR45% (Measured)
- EN1.4106, 0.71TRAM, Φ9, RR45% (Calculated)
- EN1.4106, 0.71TRAM, Φ9, RR45% (Measured)

Fig. 16. The recrystallization kinetics following the JMAK modelling; a) the non-logarithmic graph, b) the obtained computed values of the JMAK exponential power of *n*, c) the graph juxtaposed with the determination coefficient R-square in the concept of linear regression, fitting a linear model to the curves plotted, d) Logarithmic graph representing the nucleation timing in accordance with the microstructural EBSD-based IPF maps.
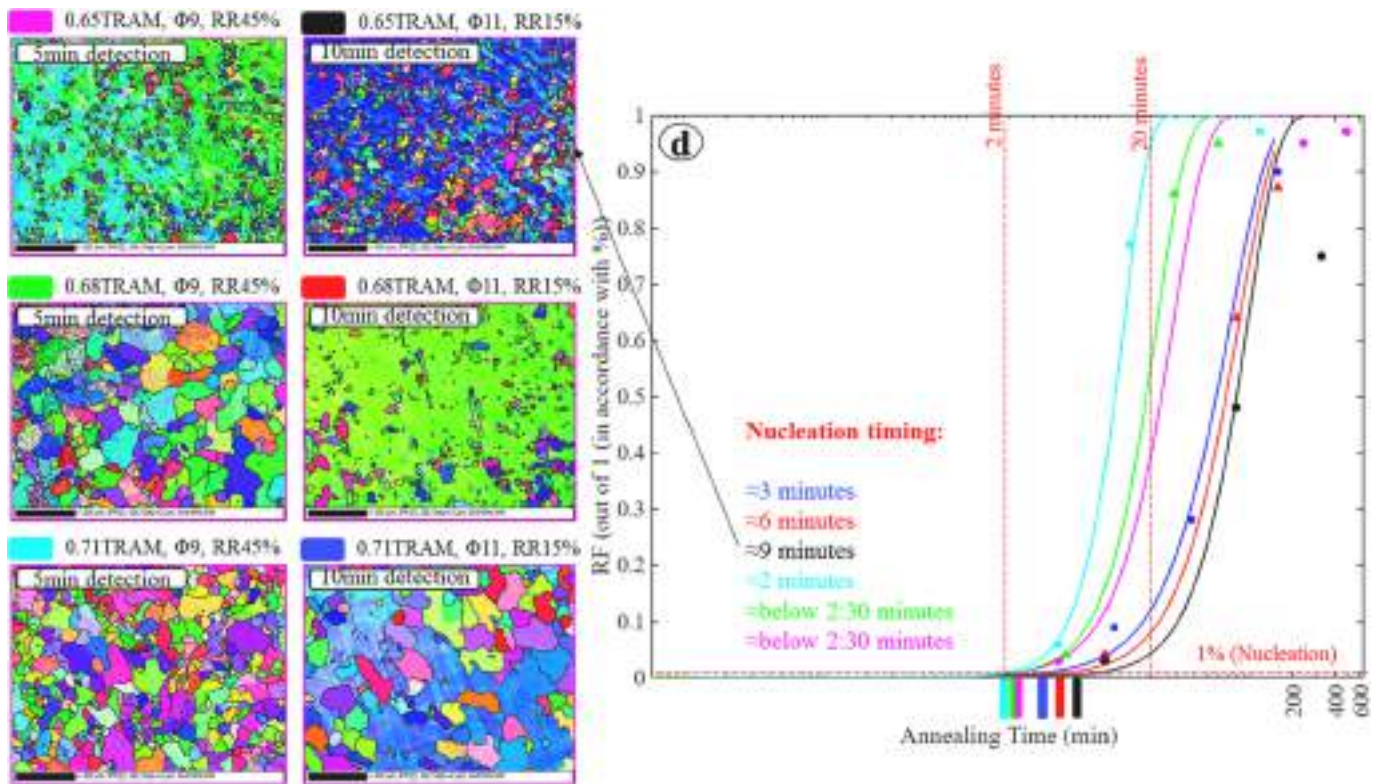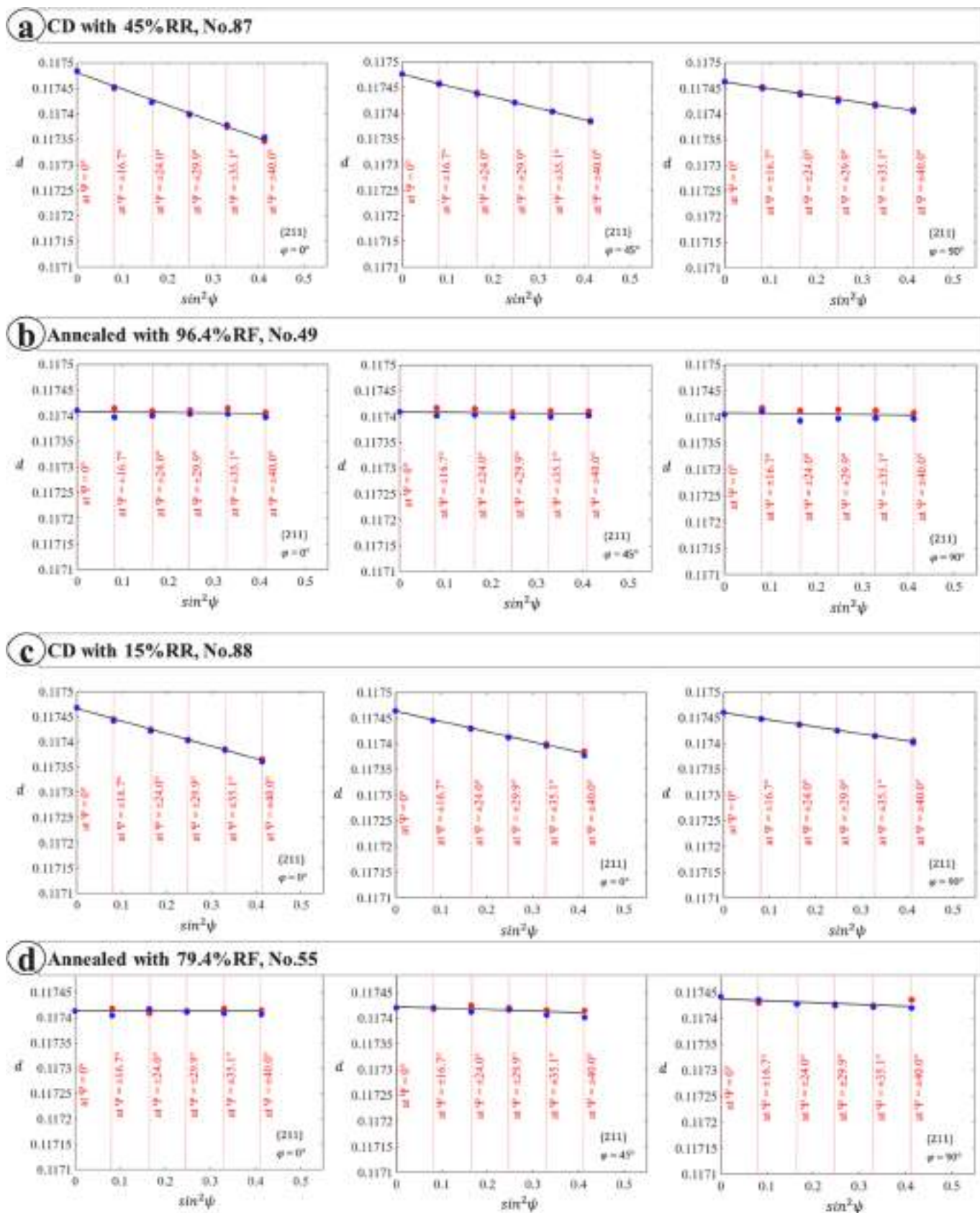
Fig. 16. (*continued*).

Fig. 17. Outputs of the fitted computed lines to experimental measured points of the interplanar distances, d, as a function of $sin^2\psi$ for a) CD with 45% RR, b) annealed with 96.4% RF, c) CD with 15% RR, and d) annealed with 79.4% RF.
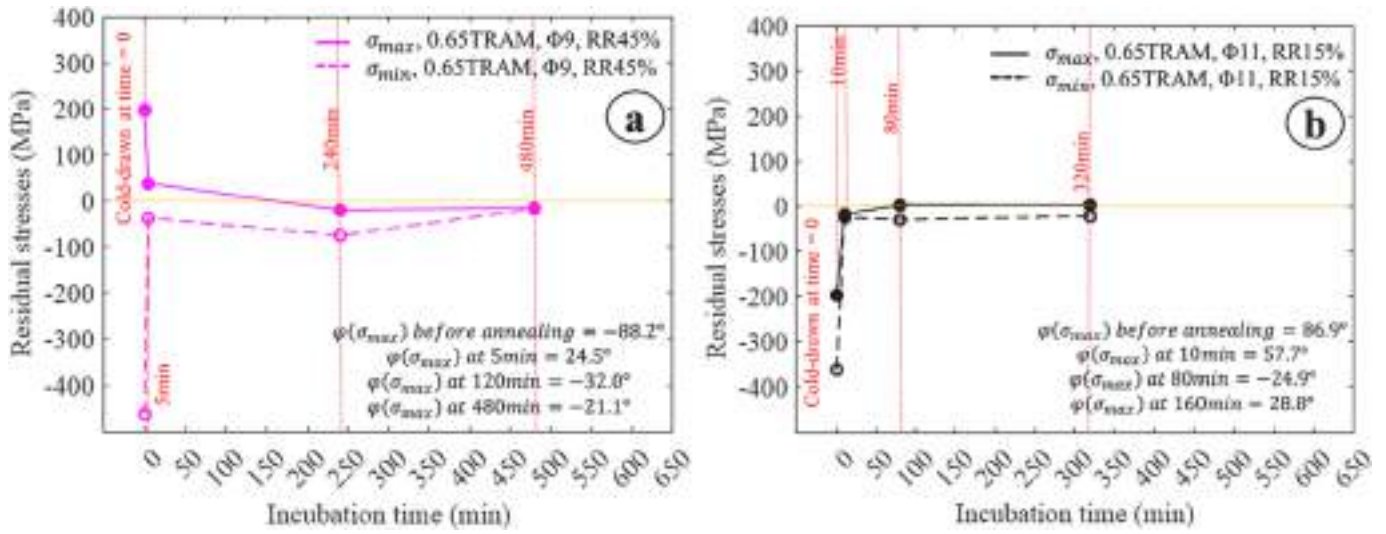
Fig. 18. Residual stresses as a function of annealing time from CD to annealed conditions for specimens of FSS under 0.65TRAM AST for a) 45% RR and b) 15% RR.
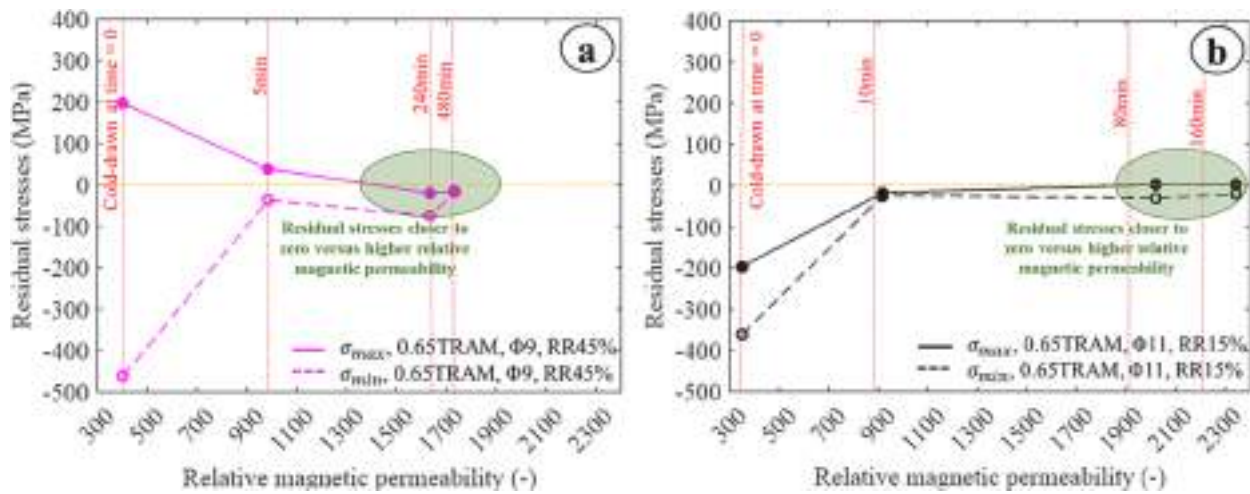

Fig. 19. Residual stresses as a function of the RMP from CD to annealed conditions for specimens of FSS under 0.65TRAM AST for a) 45% RR and b) 15% RR.
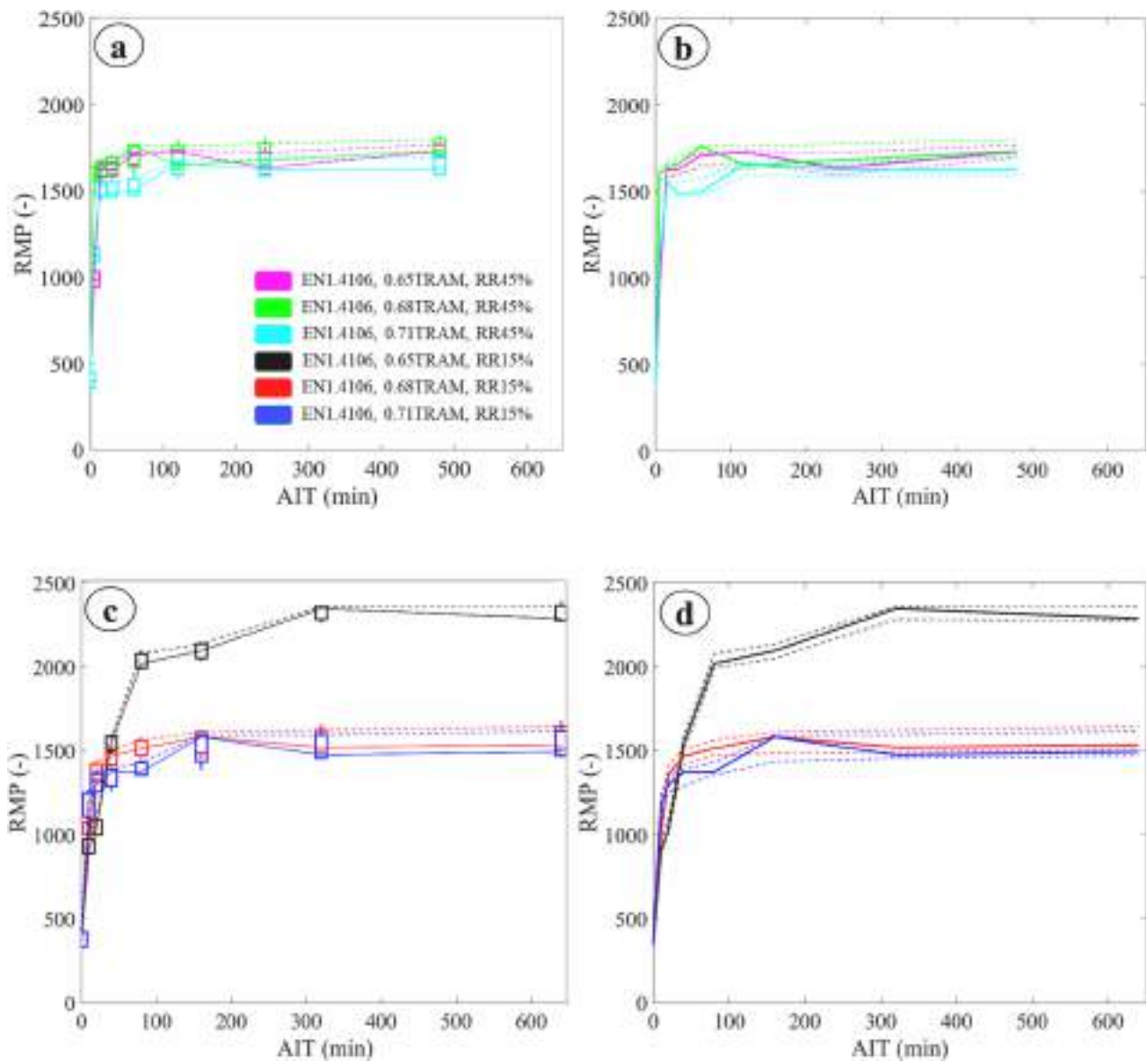
Fig. 20. RMP as a function of AIT for a) samples with 45% RR (quartile-based), b) the lines plotted among the upper quartile values, median values, and the lower quartile values for all samples with 45% RR, c) samples with 15% RR, d) the lines plotted among the upper quartile values, median values, and the lower quartile values for all samples with 15% RR, alongside samples with 45% RR: e) under 0.65TRAM, f) under 0.68TRAM, and g) under 0.71TRAM, as well as the samples with 15% RR: h) under 0.65TRAM, i) under 0.68TRAM, and j) under 0.71TRAM.
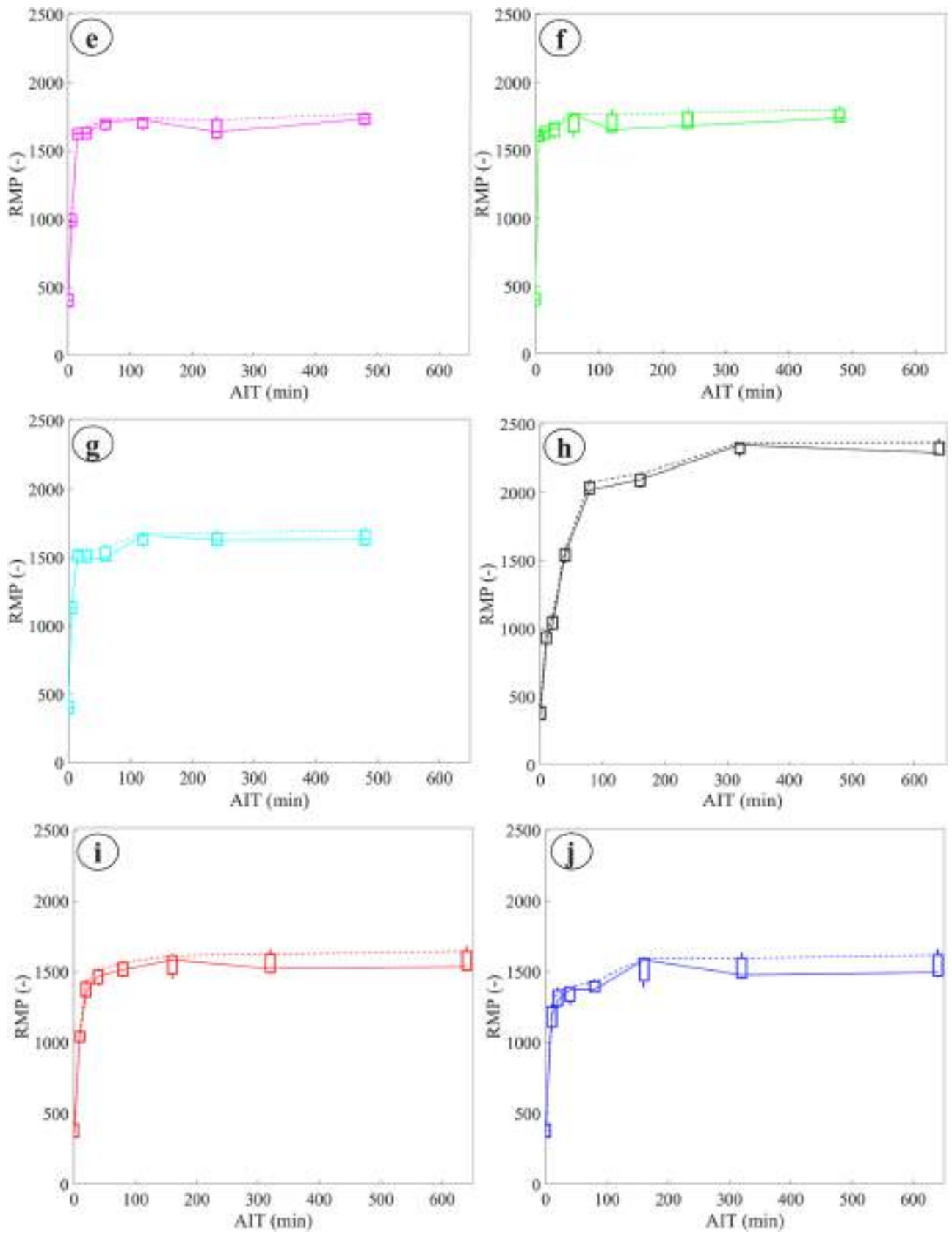
Fig. 20. (*continued*).

3.3. Residual stresses evaluation before and after heat treatment

It is evident that the measurement of residual stresses must be implemented prior to any manipulation of the samples; however, these results are reported in the end since the indication of the microstructural outputs among CD and recrystallized samples linked by residual stress outputs are essential. Moreover, the variations of stress conditions among diverse grains are basically arisen from the variations in crystallite deformations, which can be also irreversible due to the cold working process. In other words, the microstresses or intergranular stresses are generated by plastically-deformed differences among the grains.

The outcomes of 2nd order residual stress measurements respective to the microstructural analyses of the CD and heat-treated materials are signified by this section. Fig. 17 depicted these results, containing the fitted theoretical lines to the experimental measured spots for the interplanar distances, *d*, as a function of $sin^2\psi$, as the method described earlier. It is detected that the slope of them is drastically declined by the higher RF which is arisen from the higher AST and AIT. Therefore, the relaxation of the residual stresses after annealing heat treatment is remarkable.

In this section, the residual stress evolution as a function of AIT in respect to the AST represented in Fig. 18. Based on the analyses of residual stresses in Fig. 18 which has been according to the data of second-order residual stress owing to the scrutinized microstructures of the CD and heat-treated, it is important that the higher RR contributed to the larger residual stresses. To clarify, the CD FSS materials showed much higher values than stresses in the partially or fully-recrystallized specimens that have been relaxed by ISRAHT process. Nevertheless, because the scale of AST has been high enough, even over a short AIT, the stress relaxation has been perceptible. Compressive stress type, defining as negative values, normally reduces the risk of cracking on the surface layer while the tensile stress type, defining as positive ones, generally leads to initiate and even accelerate the cracking phenomenon. Referring to Fig. 19, the residual stresses would be decreased by increasing the RMP. On the other hand, the displacement of boundaries was basically impeded by large residual stresses that also displayed lower RMP and higher coercivity attributing to sharper magnetic texture.

3.4. Microstructural and textural effects on magnetic response

The magnetic behavior of such ferromagnetic material, reflecting in the hysteresis loops as shown earlier in Figs. 4 and 5, are basically influenced by several factors, namely AGS, textural orientations, defects, and the presence of secondary phases. On the other hand, the relationship among AGS, GBs, and magnetic domain walls plays a critical role in determining the magnetic behavior of a material [28]. To be exact, the smaller grain size was generally linked with enhanced magnetic properties, such as higher magnetic permeability and lower coercive force which are significant in this research in terms of the electromagnetic applications, including solenoid valves, and electrovalves. In any case, magnetic permeability, *μ*, has been an important parameter of the magnetic materials.

As for parametric investigation of magnetic behavior, Fig. 20 revealed the relationship between RMP as a function of AIT for all 44 designated specimens. Going through more details, it is quite significant to notice that the magnetic behavior could be influenced by multifaceted parameters of AGS, grains' trend, textural orientations, defects, the presence of secondary phases, AST, and AIT. The more uniform magnetic response was contributed by the finer and more equiaxed grains while, in general, the smaller grains could decrease the existence of defects and irregularities. Finer grains resulting from recrystallization annealing contributed to higher RMP and lower coercive force as a general trend which was observable in all series of Fig. 20a to j. Building upon this fact, and referring to Fig. 15 of the grains' trend, Fig. 20h of the samples with 15% RR under 0.65TRAM demonstrated the highest

values of RMP. Conversely, larger grains such as the samples in Fig. 20g showed the overall lowest RMP among the samples with 45% RR, by causing to increase the surface area of GBs compared to the smaller and finer grains. In addition, while annealing relieved the stresses of CD effects, it affected the magnetic behavior as well. Owing to Fig. 19, the specimens with lower residual stresses closer to zero arisen from annealing addressed higher RMP as well.

In another standpoint, through each set of reduction rate, the highest RMP belonged to 0.65TRAM and the lowest values came from 0.71TRAM, and, for both RRs, 0.68TRAM caused the overall median values of RMP. In other words, the magnetization in terms of overall RMP decreased as the relative homogeneous temperature increased from 0.68TRAM to 0.71TRAM. Therefore, RMP values of this FSS decreased following to further isotropy and annihilation of crystalline defects along with the other effectual parameters as above [28]. This is while the overall trend of RMP was soared up by AIT for all series.

In another standpoint, irregular GBs such as the curvaceous GBs in this study as discussed earlier, may comprise of structural defects, causing to introduce magnetic domain walls accordingly. Magnetic domain walls are called the boundaries among adjacent magnetic domains within the material. Irregular GBs could act the preferential sites for the nucleation of such magnetic domain walls. In a perfect crystal lattice, adjacent grains would have perfectly aligned atomic planes at their interface. However, in real-world materials, imperfections and deviations from ideal structures are common, and irregular GBs may arise due to various factors, containing grain growth, processing conditions, crystallographic mismatch, defects, and impurities. All in all, at irregular GBs, variations in crystallographic texture and defects could form localized regions in which the magnetization directions change, representing the magnetic domain walls.

From textural viewpoint, anisotropic properties, arisen from preferred orientation of grains, affected magnetic properties. The strong texture could display directional dependence in magnetic behavior. On the other hand, extra random or higher isotropic orientation at higher AST caused to the more uniform magnetic behavior but with further lower magnitude in all directions. However, referring to the IPF maps in Fig. 9 and pole figure maps in Fig. 13, while the comparison has been made on both 45% and 15% RR for 0.65TRAM, the influence of more uniform and higher RMP in terms of annealed samples were matched together with Fig. 20. To clarify and for instance, samples No. 49 and 55 showed the maximum median values of RMP through their series corresponding to the random and more isotropic orientation. Likewise, the presence of secondary phases, as nonmagnetic compounds, can affect the magnetic domains through introducing defects or altering the crystal structure. This would be scrutinized as further research.

4. Conclusion and future work

A mixed experimental and theoretical study on the effects of CDRR and the further required ISRAHT as well as the following SCP on the microstructures, textures, residual stresses, and magnetic properties of EN 1.4106 FSS was carried out. It is noteworthy that the JMAK theory was employed to scrutinize the behavior of this material after annealing by utilization of the EBSD-based experimental data analyses. In this regard, the below remarks are concluded:

- The increasing enforcement of CDRR from 15% to 45% caused to faster recrystallization formation with the refinement of microstructures and textures as well. This is while the influence of AST and AIT were monitored by the process although the playing role of annealing temperature is evidently more significant and determinative than time. Taking the example based on the JMAK modelling, within 20 min of annealing process, around 96% RF was achieved by 0.71TRAM AST for 45% RR versus around 4% of RF obtained by 0.65TRAM with 15% RR. This was the evaluation of the CDRR effect on the RF by considering the mutual effect of AST. All in all, the

variations of the recrystallized grains were directly proportional and insensitive to CDRR.

- The soonest nucleation initiation was belonged to higher RR of 45% under highest AST at 0.71TRAM within only 2 min whereas the latest newly-formed grains were occurred by 15% RR under the lowest AST of 0.65TRAM within 9 min.

- This aforesaid higher CDRR clearly led to affect the formation of more fragmented grains and more consequential LAGBs. With such an increment in CDRR, the AGS decreased accordingly. For instance, concerning the center area of the specimens, the AGS was 35.37 μm under 0.65TRAM AST after 480 min for 45% RR while this value was 42.74 μm under same AST and only after 320 min for 15% RR.

- By engendering the HAGBs which are favorable to enhance the mechanical behavior of the material, the determinative role of the movement from LAGB to HAGB through the CD to fully recrystallized samples are another noticeable aspect.

- From textural standpoint, the recrystallization led to the formation of new grains with wider preferred orientations or alignment, resulting in the more well-pronounced texture in terms of lower MUD values and even with more clusters. The strongest tendency for orientations is the plane family {1 0 0} that exhibited more dense clusters from CD to recrystallized specimens corresponding to the RD. Moreover, it was noticeable that for the CD samples the textural preference contributed to ⟨1 1 1⟩ towards ⟨1 0 1⟩ specifically in the center corresponding to the grains' elongation into the RD while the annealed samples did not specify a strong tendency (that is also compatible with PF) since the newly-formed grains during the recrystallization were replaced by the deformed grains. That is the reason why they had the wider range of orientations depending on different factors such as the nucleation sites. Referring to the ODF contour maps, the CD samples were mainly consisted of the α-fibre texture close to {2 2 3} ⟨1 1 0⟩ and {1 1 1} ⟨1 1 0⟩ orientations whereas, by higher recrystallization fractions, the texture tendency by formation of γ-fibre was close to {1 1 1} ⟨0 1 1⟩ orientation resulting in more spread of texture with lesser intensity in compared to CD state.

- The effectual factors on the magnetic behavior of this grade were AST, AIT, and RR by the priorities. To be more exact, the higher fraction of recrystallized grains, which were formed by the appropriate AST and AIT, showed the least scale of residual stresses in compared to the CD unheated materials while the magnetic properties have been followed by the same behavior. The interaction behavior of residual stresses and residual magnetization is another aspect of this research for our future work.

- A complex interplay of parameters, including AGS, grain morphology, textural orientations, defects, AST, and AIT were studied to investigate magnetic response. Finer and more equiaxed grains resulting from recrystallization annealing generally contributed to the higher RMP and lower coercive force. Conversely, larger grains showed lower RMP due to increased grain boundary surface area. Anisotropic properties from grain orientation exhibited directional dependence in magnetic behavior, while higher AST resulted in the more uniformly magnetic response, the critical AST of 0.68TRAM was revealed as the maximum overall RMP.

- Moreover, the fully-annealed EN1.4106 FSS with magnetic hysteresis optimized the low-scale values of coercivity of approximate 180 A/m to 220 A/m with the range of RMP of around 1500 to 2300. To be more exact, the average values of RMP and coercive force were obtained by 1900 ± 300 and 200 ± 20 A/m for the approximately fully annealed specimens opposed to 370 ± 30 and 620 ± 40 A/m for CD ones, indicating softer material by higher RMP and lower coercivity. However, the resistance to corrosion and mechanical behavior is vital to be evaluated as the further research under processing.

5. Data availability

The raw data required to reproduce these findings will be made available on request. Also, in this case, the processed data will be made available on request.

CRediT authorship contribution statement

Shahab Bazri: Conceptualization, Data curation, Formal analysis, Investigation, Methodology, Resources, Software, Validation, Visualization, Writing – original draft, Writing – review & editing. **Carlo Mapelli:** Conceptualization, Methodology, Project administration, Supervision, Validation, Writing – review & editing. **Silvia Barella:** Conceptualization, Formal analysis, Supervision, Validation, Writing – review & editing. **Andrea Gruttadauria:** Conceptualization, Methodology, Software, Writing – review & editing. **Davide Mombelli:** Conceptualization, Methodology, Resources. **Renato Nemfardi:** Conceptualization, Methodology, Resources. **Roberto Bedini:** Project administration, Resources, Software. **Giorgio Zucchelli:** Project administration, Resources.

Declaration of competing interest

The authors declare the following financial interests/personal relationships which may be considered as potential competing interests: Shahab Bazri reports equipment, drugs, or supplies was provided by Eure Inox srl. If there are other authors, they declare that they have no known competing financial interests or personal relationships that could have appeared to influence the work reported in this paper.

Data availability

The data that has been used is confidential.

References

[1] T.M. Krishnan, C. Balamurugan, I. Dinaharan, R. Palanivel, Influence of arc duration on microstructure and tensile behavior of magnetically impelled arc butt welded AISI 409 ferritic stainless steel tubes, Mater. Sci. Eng. A 831 (April 2021) (2022) 142257, https://doi.org/10.1016/j.msea.2021.142257.

[2] L. Ma, S. Hu, J. Shen, J. Han, Z. Zhu, Effects of Cr Content on the Microstructure and Properties of 26Cr-3.5Mo-2Ni and 29Cr-3.5Mo-2Ni Super Ferritic Stainless Steels, J. Mater. Sci. Technol. 32 (6) (2016) 552–560, https://doi.org/10.1016/j.jmst.2016.03.022.

[3] X. Zhang, L. Fan, Y. Xu, J. Li, X. Xiao, and L. Jiang, "Texture, microstructure and mechanical properties of aluminum modi fi ed ultra-pure 429 ferritic stainless steels," JMADE, vol. 89, pp. 626–635, 2016, 10.1016/j.matdes.2015.09.147.

[4] S.K. Gupta, A.P. Patil, R.C. Rathod, V. Tandon, A. Gupta, J. Chavhan, Influence of filler variation on microstructural evolution, mechanical and corrosion performance of Ti-stabilized 439 ferritic stainless steel, Mater. Today Commun. 34 (November 2022) (2023) 105010, https://doi.org/10.1016/j.mtcomm.2022.105010.

[5] M. Jiang, et al., Microstructural characterization of aging precipitation behavior of, Mater Charact 171 (November 2020) (2021) 110779, https://doi.org/10.1016/j.matchar.2020.110779.

[6] H. Li, T. Zhu, N. Takata, M. Kobashi, M. Yoshino, Effect of trace solute titanium on plastic deformation of α-(Fe, Cr) single-crystal micropillars fabricated from 18Cr ferritic stainless steel, Mater. Sci. Eng. A 803 (September 2020) (2021) 140455, https://doi.org/10.1016/j.msea.2020.140455.

[7] M. Jiang, Y. Han, J. Sun, J. Sun, G. Zu, H. Chen, Precipitation of Cu- and Nb-rich phases and its strengthening effect in 17Cr ferritic stainless steel during high-temperature creep process, Mater Charact vol. 179, no. April (2021) 111346, https://doi.org/10.1016/j.matchar.2021.111346.

[8] Y. Bai, T. He, Y. Liu, Effects of Sn microalloying on cold rolling and recrystallization textures and microstructure of a ferritic stainless steel, Mater Charact 137 (September 2017) (2018) 142–150, https://doi.org/10.1016/j.matchar.2018.01.022.

[9] L. Jacquet, R. Estevez, M. Braccini, M. Libert, N. Meyer, M. Mantel, Study of cleavage fracture in ferritic stainless steels Part II: Cleavage micro-mechanisms and critical stresses, Mater. Sci. Eng. A vol. 866, no. January (2023) 144660, https://doi.org/10.1016/j.msea.2023.144660.

[10] L. Jacquet, et al., Study of Cleavage Fracture in Ferritic Stainless Steels - Part I: Development and Characterization of Model Microstructures, Mater. Sci. Eng. A 864 (December) (2022) 2022, https://doi.org/10.2139/ssrn.4264398.

[11] H. H. Lu, H. K. Guo, and W. Liang, "The dissolution behavior of σ-phase and the plasticity recovery of precipitation-embrittlement super-ferritic stainless steel," *Mater. Charact.*, vol. 190, no. March, p. 112050, 2022, 10.1016/j.matchar.2022.112050.

[12] G. Cai, C. Li, D. Wang, Y. Zhou, Investigation of annealing temperature on microstructure and texture of Fe-19Cr-2Mo-Nb-Ti ferritic stainless steel, Mater Charact 141 (April) (2018) 169–176, https://doi.org/10.1016/j.matchar.2018.04.031.

[13] C. Liu, et al., Dynamic recrystallization behavior under steady and transient mutation deformation state, Mater. Sci. Eng. A vol. 843, no. April (2022) 143138, https://doi.org/10.1016/j.msea.2022.143138.

[14] X. Sun, X. Ma, J. Li, L. Ma, M. Zhang, and J. Zhao, "The effect of cold rolling reduction ratio on the microstructure and mechanical properties of ferritic stainless steel 430," *Int. J. Adv. Manuf. Technol.*, no. 0123456789, 2023, 10.1007/s00170-023-11159-w.

[15] B. Mishra, et al., Effect of Cold Rolling and Subsequent Heat Treatment on Microstructural Evolution and Mechanical Properties of Fe-Mn-Al-C-(Ni) Based Austenitic Low-Density Steels, Mater. Sci. Eng. A vol. 861, no. June (2022) 144324, https://doi.org/10.2139/ssrn.4141250.

[16] H. Li, M. Li, Z. Cai, L. Ma, Y. Ma, Microstructure evolution, tensile properties and deformation mechanism of Fe-6.5 wt.% Si steel doped with yttrium, Mater. Sci. Eng. A vol. 859, no. September (2022) 144216, https://doi.org/10.1016/j.msea.2022.144216.

[17] H.F.G. De Abreu, A.D.S. Bruno, S.S.M. Tavares, R.P. Santos, S.S. Carvalho, "effect of High Temperature Annealing on Texture and Microstructure on an AISI-444 Ferritic Stainless Steel" 57 (2006) 342–347, https://doi.org/10.1016/j.matchar.2006.02.015.

[18] R. Wawszczak, et al., Evolution of microstructure and residual stress during annealing of austenitic and ferritic steels Compressive versus tensile stresses, Mater Charact i (2016) 238–251, https://doi.org/10.1016/j.matchar.2015.12.019.

[19] C. Mapelli, et al., JMAK model applied on the κ-carbide precipitation in FeMnAlC steels, J. Mater. Res. Technol. 15 (2021) 3386–3398, https://doi.org/10.1016/j.jmrt.2021.09.139.

[20] W.A. Johnson, R.F. Mehl, Reaction kinetics in processes of nucleation and growth, Trans. AIME 135 (1939) 416–458.

[21] M. Avrami, Kinetics of phase change. I. General theory, J. Chem. Phys. 7 (1939) 1103–1112.

[22] A.N. Kolmogorov, Statistical theory of crystallization of metals, Izv. Ross. Akad. Nauk. Seriya Mat. 1 (1937) 355–359.

[23] S. Bazri, et al., Microstructural, textural, and residual stress evolution alongside the magnetic properties through isothermal static recrystallization of cold-drawn Fe e Cr e Si e S e C ferritic high-alloy stainless steel and by JMAK modelling, J. Mater. Res. Technol. 23 (2023) 3091–3118, https://doi.org/10.1016/j.jmrt.2023.01.216.

[24] C.G. Kang, J.W. Yoon, "Effect of Strain Localization on the Mechanical Properties from Nonuniform Grain Size Distribution of, Ultralow Carbon Steel" 2200335 (2022) 1–9, https://doi.org/10.1002/srin.202200335.

[25] T. Matsui, T. Ogawa, Y. Adachi, Relationship between three-dimensional microstructure and Avrami exponent for recrystallization in pure iron, Results Mater. vol. 1, no. June (2019) 100002, https://doi.org/10.1016/j.rinma.2019.100002.

[26] J. W. Cahn, "No Title," *Acta Metall. Mater.*, vol. 449, no. 4, 1956.

[27] C.W. Price, Use of Kolmogorov-Johnson-Mehl-Avrami kinetics in recrystallization of metals and crystallization of metallic glasses, Acta Metall. Mater. 38 (5) (1990) 727–738, https://doi.org/10.1016/0956-7151(90)90024-B.

[28] A. N. Acar, D. Kaya, A. K. Ekşi, and A. Ekicibil, "Pressure effect on the structural, magnetic and thermophysical properties of X12Cr13 martensitic stainless steel prepared by powder metallurgy method," *Mater. Today Commun.*, vol. 33, no. November, 2022, 10.1016/j.mtcomm.2022.104924.